AERODYNAMIC AND INERTIAL CHARACTERIZATION OF A GENERIC FLAPPING WING MECHANISM

A THESIS SUBMITTED TO
THE GRADUATE SCHOOL OF NATURAL AND APPLIED SCIENCES
OF
MIDDLE EAST TECHNICAL UNIVERSITY

BY

CAN BEKER

IN PARTIAL FULFILLMENT OF THE REQUIREMENTS
FOR
THE DEGREE OF MASTER OF SCIENCE
IN
AEROSPACE ENGINEERING

SEPTEMBER 2020

Approval of the thesis:

AERODYNAMIC AND INERTIAL CHARACTERIZATION OF A GENERIC FLAPPING WING MECHANISM

submitted by **CAN BEKER** in partial fulfillment of the requirements for the degree of **Master of Science in Aerospace Engineering, Middle East Technical University** by,

Prof. Dr. Halil Kalıpçılar
Dean, Graduate School of **Natural and Applied Sciences**

Prof. Dr. İsmail Hakkı Tuncer
Head of the Department, **Aerospace Engineering, METU**

Prof. Dr. Dilek Funda Kurtuluş
Supervisor, **Aerospace Engineering, METU**

Assist. Prof. Dr. Ali Emre Turgut
Co-Supervisor, **Mechanical Engineering, METU**

Examining Committee Members:

Prof. Dr. Ozan Tekinalp
Aerospace Engineering, METU

Prof. Dr. Dilek Funda Kurtuluş
Aerospace Engineering, METU

Assist. Prof. Dr. Ali Emre Turgut
Mechanical Engineering, METU

Assist. Prof. Dr. Kutluk Bilge Arıkan
Mechanical Engineering, TED Uni.

Assist. Prof. Dr. Onur Özcan
Mechanical Engineering, Bilkent Uni.

Date: 10.09.2020

I hereby declare that all information in this document has been obtained and presented in accordance with academic rules and ethical conduct. I also declare that, as required by these rules and conduct, I have fully cited and referenced all material and results that are not original to this work.

Name, Last name : Can Beker

Signature :

ABSTRACT

AERODYNAMIC AND INERTIAL CHARACTERIZATION OF A GENERIC FLAPPING WING MECHANISM

Beker, Can
Master of Science, Aerospace Engineering
Supervisor: Prof. Dr. Dilek Funda Kurtuluş
Co-Supervisor: Assist. Prof. Dr. Ali Emre Turgut

September 2020, 85 pages

The primary focus of this thesis is to conduct an aerodynamical and inertial characterization of a generic flapping wing mechanism. Firstly, a CAD model of the utilized flapping mechanism is created, and a custom test platform is developed for the performed flapping-wing test sequence. Experimental validation of the modal analysis performed for the developed test platform is presented. In the inertial force characterization study, the standalone effect of the inertial forces that occur during flapping motion on the produced total aerodynamic lift force is aimed to investigate. In this framework, the wing membrane is eliminated, and a flapping wing test is performed to measure the inertial force generated due to the motion of the prescribed kinematics in the lift direction. The dynamic calibration of the utilized sensor is carried out to ensure the fidelity of the acquired data during the flapping test. Verification studies regarding to the experimental inertial force investigation are conducted by performing theoretical and dynamic finite element analysis approaches. For the aerodynamic characterization of the proposed system, a nylon wing membrane is attached to the utilized flapping wing mechanism, and a flapping wing experiment is performed in the air medium. To verify the experimental results, a numerical validation study is conducted and, a fluid-structure interaction analysis model is presented for the corresponding model. Besides, the effect of wing-flexion on aerodynamic performance is investigated for the corresponding model. In this regard, a distinct fluid-structure interaction analysis model, including a flapping wing with high-rigidity material properties, is created to minimize the deflection that occurs on the wing structure.

Experimental, theoretical, and numerical approaches conducted for the inertial and aerodynamic characterization of the utilized flapping mechanism showed great resemblance to each other. A comparative study performed for the effect of wing-flexion shows that wing elasticity enhances the thrust force for the proposed model.

Keywords: Flapping Wing, Micro Air Vehicles, Dynamic Finite Element Analysis, Fluid-Structure Interaction Analysis, Computational Fluid Dynamics

ÖZ

JENERİK BİR ÇIRPAN KANAT MEKANİZMASININ AERODİNAMİK VE ATALET KARAKTERİZASYONU

Beker, Can
Yüksek Lisans, Havacılık ve Uzay Mühendisliği
Tez Yöneticisi: Prof. Dr. Dilek Funda Kurtuluş
Ortak Tez Yöneticisi: Dr. Öğr. Üyesi Ali Emre Turgut

Eylül 2020, 85 sayfa

Bu tezin ana odağı jenerik bir çırpan kanat mekanizmasının aerodinamik ve atalet karakterizasyonunu gerçekleştirmektir. İlk olarak, kullanılan çırpan kanat mekanizmasının üç boyutlu modeli oluşturulmuş ve gerçekleştirilen çırpan kanat deneysel çalışması yeni bir test fikstürü sunulmuştur. Modal analizi gerçekleştirilen, test fikstürünün deneysel doğrulaması gerçekleştirilmiştir. Atalet karakterizasyon çalışmasında, çırpma hareketi esnasında oluşan atalet kuvvetlerinin, aerodinamik kaldırma kuvvetlerine olan etkisinin araştırılması amaçlanmıştır. Bu çerçevede, kanat membranı ihmal edilmiş ve çırpan kanat testi, mekanizmanın kaldırma kuvveti yönünde oluşturduğu atalet kuvvetlerinin ölçümü için gerçekleştirilmiştir. Gerçekleştirilen çırpan kanat testinden elde edilen verilerin doğrulundan emin olmak için kullanılan kuuvet sensörüne ait dinamik kalibrasyon çalışması gerçekleştirilmiştir. Deneysel yöntemle elde edilen atalet kuvvetlerinin doğrulama çalışması, nümerik ve teorik yaklaşımlarla gerçekleştirilmiştir. Kullanılan çırpan kanat kanat mekanizmasının aerodinamik karakterizasyonu için, naylon bir kanat membranı çırpan kanat mekanizmasının üzerine yerleştirilmiş ve hava ortamında çırpan kanat testleri gerçekleştirilmiştir. Deneysel sonuçların doğrulaması için, sıvı-katı etkileşimli analiz modeli oluşturularak hesaplamalı akışkanlar dinamiği (laminar akış) modeli ve yapısal dinamik modeli eş zamanlı çözdürülmüştür. Bunun yanında, kanat esnekliğinin aerodinamik performansa olan etkisi araştırılmıştır. Bunun için

kanat yapısına yüksek rijitliğe sahip bir malzeme tanımlanarak kanat deplasmanının minimize edilmesi amaçlanmış, ve esnek ve rijit kanat performansı kaldırma ve itki kuvveti için karşılaştırılmıştır.

Bu çalışmada, jenerik bir çırpan kanat mekanizmasının, test, teori ve nümerik yaklaşım ile aerodinamik ve atalet karakterizasyonunun karşılaştırmalı doğrulama çalışması sunulmuştur ve yakın sonuçlar elde edilmiştir. Kanat esnekliğinin aerodinamik performansa olan etkisi için yapılan karşılaştırmalı çalışmada, kanat esnekliği aerodinamik itki kuvvetini gözle görülür derecede arttırarak tam itki durumu oluşturmuştur.

Anahtar Kelimeler: Çırpan Kanat, Mikro Hava Aracı, Dinamik Sonlu Elemanlar Analizi, Sıvı-Katı Etkileşimli Analiz, Hesaplamalı Akışkanlar Dinamiği

To my family…

ACKNOWLEDGMENTS

I would like to thank my thesis advisor Prof. Dr. Dilek Funda Kurtuluş, for her precious help, guidance throughout my thesis study. I am extremely grateful to work with her for contributions and caring for my ideas to make my study productive.

My sincere gratitude is reserved for Asst. Prof. Ali Emre Turgut, who gave me support whenever I was struggling with my thesis and willing to collaborate during my challenge.

I would like to extend my sincere thanks to METU Aerospace Aerodynamics Lab. members for their precious support and collaboration throughout my master's study.

I want to thank wholeheartedly my parents, Nuri and Selma, and my brothers, Levent and Cem. This study wouldn't be possible without their genuine love and care, and their never-ending confidence and support in me.

I'd like to present my sincere thankfulness to my dear deceased uncle Soner Beker who died in September 2019 for his unconditional help throughout my master's study and experience in Ankara.

The corresponding research study is funded by the Scientific and Technological Research Council of Turkey under grant number TUBITAK 116M273. I would like to thank them for providing me financial support and gave me the opportunity to present my research in a high-level conference via the 2224-A program.

I hope the proposed study enlightens the way of the future laboratory members or researchers from any part of the world who wish to work on the corresponding subject and desire to contribute to science and utilize it for the sake of humanity.

TABLE OF CONTENTS

LIST OF TABLES

TABLES

LIST OF FIGURES

FIGURES

CHAPTER 1

INTRODUCTION

1.1 Background

Recently, small-scaled aircraft have gained a significant role in various areas, such as military and civilian applications. The definition of micro air vehicle is given by DARPA for the first time as tiny scale aircrafts smaller than 15 cm of wingspan [1]. Micro air vehicles are preferred to utilize in certain types of tasks where unobtrusive and invisibility are the priority of the conducted operation. MAVs offer a suitable platform to collect data in hard-to-access places such as combat, hazardous, and collapsed buildings regions. Micro air vehicles broaden the agility and quickness limitations performed by macro-scale aircraft and terrestrial robots. They show far better performance in terms of signaling-based localization and overcoming obstacles such as barriers and stairs, especially for indoor applications. MAVs are an emerging research area, and lots of research and infrastructure investments are made under government and industrial projects to provide quality service in military and civilian applications to exploit from the benefits of the small-scale piloting. As a consequence, the number of scientific activities is boosted up, and researchers over the decades proposed many studies. Figure 1.1 illustrates the number of published academic papers in the MAVs field registered to the Web of Science database in the last 25 years [2].

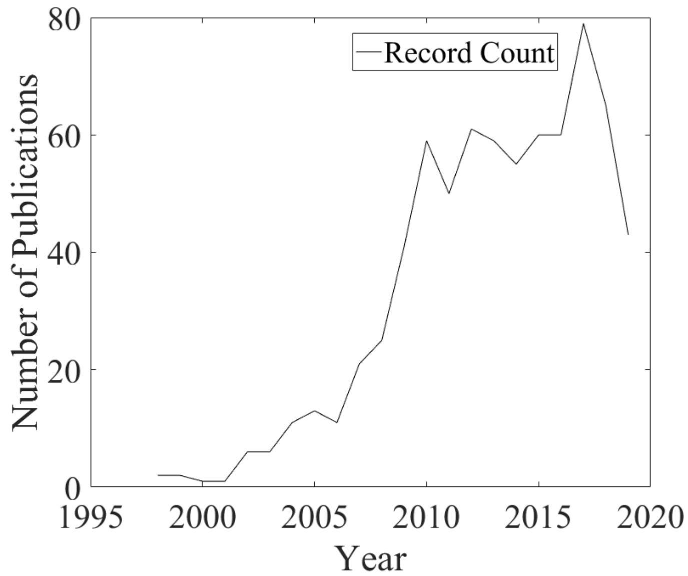

Figure 1.1: Number of publications seen during the last 25 years [2]

Micro air vehicles research area is a multilayered research field and embodies the various types of design options that have been engineered and proposed, including fixed-wing, rotary-wing, and flapping-wing types of MAVs. Fixed-wing flight has the same characteristic as conventional fixed-wing aircraft. Rotary wing MAVs show similar characteristics to helicopter flight and maintain its flight through the rotation of the blades. The flapping flight mimics the biological creatures and performs pitching and plunging motion to maintain its flight condition. The flapping wings prevail certain assets over conventional platforms acting as a bird and offering hovering, gliding, and perching in a compact design. The flapping flight dominantly possesses a complex aerodynamic characteristic that distinguishes from conventional aircraft. FWMAVs use the low-Reynolds number regime from 10^1 to 10^5 and deals with the unsteady characteristic of the airflow. Over the past decade, numbers of researchers engineered bio-inspired natural flyers [3-8], as given in Figure 1.2.

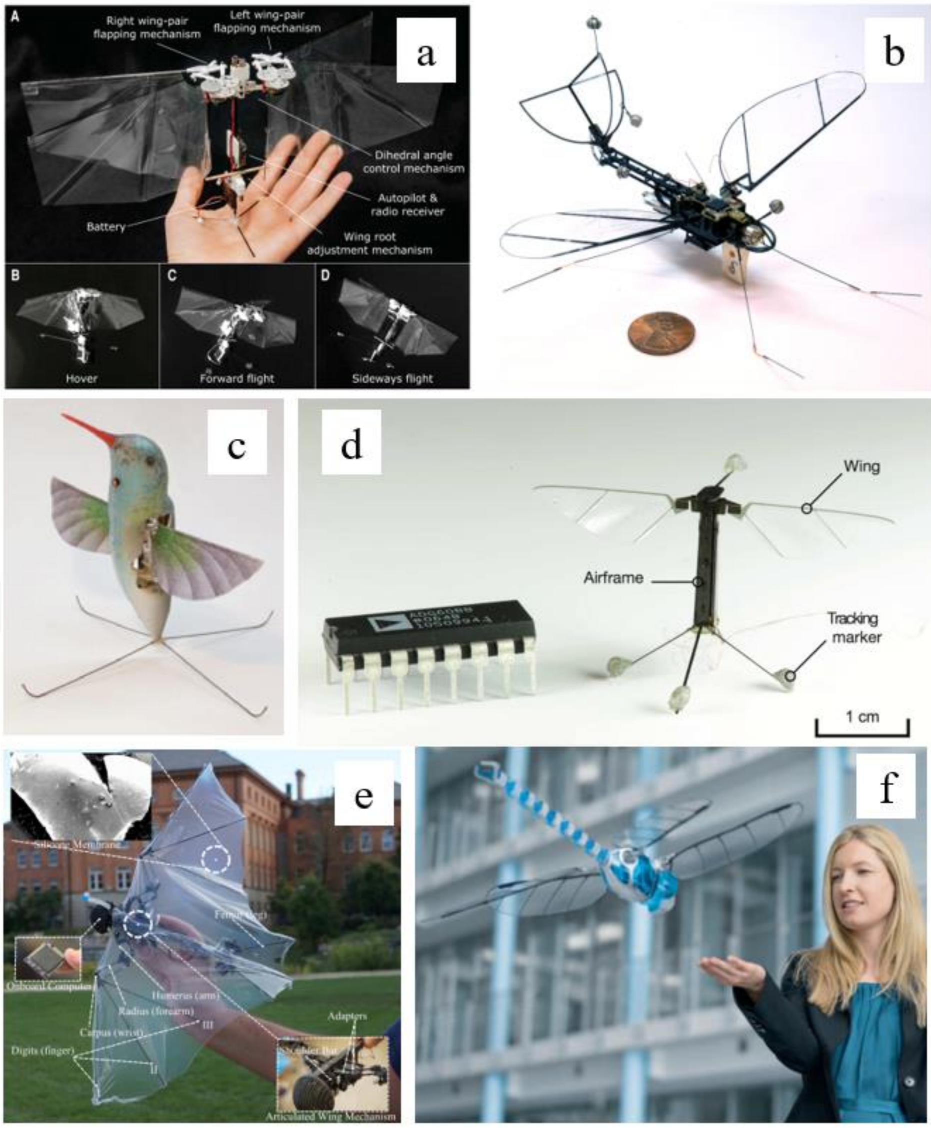

Figure 1.2: Developed flapping-wing micro air vehicles a) [3] b) [4] c) [5] d) [6] e) [7] f) [8]

1.2 Objective and Thesis Outline

The objective of this thesis is to design a flapping wing test stand and to validate experimental force measurement results with theoretical and numerical approaches. In a recent study performed in the METU Aerospace Engineering Department Aerodynamics Lab., a test stand was developed for a scaled blowfly wing, and verification studies for the flapping-wing test are carried out [9]. A four-bar link mechanism, along with a servo motor, is utilized as a mechanical flapper to create a beating motion for the experimental purpose. The resultant lift force obtained in the experimental study is compared with the numerical and theoretical results and presented. However, the corresponding study performed by Senol [9] suffers from certain assets such as neglecting the wing elasticity and the inertial forces generated by the linkages of the utilized four-bar mechanism. Conceptual-wise, the present study is based on the abovementioned study [9] with a different architecture such as mechanism, wing, and frequency. Furthermore, the rigid-body dynamics calculations are performed in a more detailed form, and aeroelastic analysis method is utilized. Also, design steps regarding the proposed custom test stand compliant with the utilized flapping mechanism along with CAD models, modal characterization, and sensor calibration phases are presented. The flapping tests are conducted for the inertial (without wing membrane), and aerodynamic (with wing membrane) characterization of the proposed flapping mechanism and reported concordantly.

Before conducting the current master thesis, several studies are performed previously based on distinct flapping models [10,11]. Those studies can be attributed to the milestones of the proposed thesis study, and the methodological experience gained from the aforementioned studies is traced along throughout the proposed master thesis study.

The presented study is organized into five chapters.

Chapter 1 includes background information about FWMAV and the objective of the current thesis.

In Chapter 2, performed numerical and experimental studies for the flapping systems in literature are presented.

Chapter 3 elaborates on the methodology that covers the inertial and aerodynamic characterization of the flapping mechanism employed in the proposed study.

Chapter 4 presents the results associated with the methods carried out in Chapter 3. Experimental, theoretical, and numerical results obtained for the inertial and aerodynamic characterization studies for the proposed flapping mechanism are presented comparatively. Also, the wing-flexion impact on aerodynamic performance is questioned. In this framework, a flapping wing model with high-rigidity material properties is created, and the corresponding developed flow structures compared to the flow structures occurred on the elastic wing model.

A broad conclusion related to performed experimental, numerical, and theoretical studies performed for the inertial and aerodynamic characterization of the utilized flapping wing mechanism is given in Chapter 5.

CHAPTER 2

LITERATURE SURVEY

2.1 Numerical Studies

Research on micro air vehicles (MAVs) is a thriving area of interest that is being conducted by many researchers with the progress in the performance of the computational tools utilized to understand the unsteady aerodynamic behavior. Many researchers performed various studies to understand how small-scaled flapping flyers generate a sufficient level of lift and thrust forces. On the contrary of the conventional aircraft, flapping-wing flyers are operated in low Reynolds number regime (O~10^4). Researchers showed that the operating in low Reynolds number regime cause to decrease lift-to-drag ratios, increase drag coefficient magnitudes with high sensitivity observation at inflow transition and separation characteristic [12]. For the augmentation of the lift force, flapping-wing designs exploit the leading-edge vortex mechanism to achieve large forces [13]. Not only for flapping wing flyers, but the LEV mechanism has also been investigated and presented in other unsteady aerodynamics utilizing delta wings in conventional aircraft systems to enhance their lift production capacity [14-15]. In this framework, many studies can be attributed to the potential of the lift generation capability, aerodynamic performance exhibited by the LEV mechanism. However, LEV phenomena only occur for a short time interval of the flapping stroke, and it visually appears at the end of up and downstroke. There is still a limited understanding of the behavior of leading-edge vortex that influences aerodynamic force production.

Some primary studies have been put forward to show the effect of LEV formation occurred on flapping wings undergoing pitching and plunging motion using 2D numerical methods. Hamdani and Sun [16] present the essence of flapping-wing aerodynamics by employing 2D numerical analysis for an insect wing. A CFD model is created along with a flapping wing that performs translational acceleration, deceleration, and rapid pitching up between 0° and 60° degrees in a constant free-stream, which is suitable for small insects (Re=0(100)). The corresponding research claims when the airfoil acting a rapid pitching motion when undergoes a constant stream, flapping-wing in low Reynolds number performs as effective as in high Reynolds number regime. As a consequence, the majority of the aerodynamic lift force is produced in fast pitching motion while undergoing a constant free stream. Researchers put forward a 2D numerical study to explore the characteristics of NACA0012 airfoil with 100 mm thickness experiencing a plunging motion at a zero angle of incidence and zero free stream velocity [17]. The corresponding study aims to understand how the NACA0012 airfoil exploits the unsteady mechanisms to produce thrust force. Also, a comparative study is offered to understand the impact of airfoil shape on the aerodynamic performance, and the propulsive performance difference between NACA0012 airfoil and a simple cylindrical structure in plunging motion is investigated. Several milestone studies are carried out to enlighten the effect of flexion on the aerodynamic performance of flapping wings. Deng and Xiao [18] performed a 2D numerical analysis to investigate the chord-wise flexibility on the propulsive performance of the utilized wing-section. An in-house developed Navier-Stokes solver is employed to run flexible wing analysis. It is reported that the chord flexion has a positive impact on the propulsive characteristic of the wing section. In addition to the chord flexion, [19] enlighten the effect of flapping frequency effect on thrust production of flapping wings. It is shown that the resonant frequency allows the utilized flapping-wing model to reach its maximum propulsion force generation level. However, the optimum propulsive efficiency is obtained when the flapping wing is operated at about half of the resonance frequency.

Many flapping wing flyers tend to increase the wing amplitude to generate more lift force at once. Clapping technique is a widely used method by flapping wing flyers to boost up the generated lift force during flapping motion. This technique lets the trailing edge of both right and left wings nearly touch each other when the wings pronate. Increasing the wing amplitude arise to develop complex flow structures around the wing surface. Therefore, 3D CFD solvers are utilized to analyze more complex flows generated by the flapping wings. Kolomenskiy et al. [20] investigate the performance difference between 2D and 3D numerical wing models and a good qualitative agreement between 3D analysis, and experimental results attained compared to 2D model results. [21]. Liu and Kawachi [21] published the first notable 3D numerical flapping-wing study that encompasses comparative experimental studies. In this study, a morphologically and kinematically mimicking Manduca Sexta wing is simulated and compared to the conducted experimental results. It is pointed out that the performed analysis results show a great deal of agreement with the smoke visualization test, and the LEV mechanism provides a great deal of lift enhancement. Another notable research study about the utilization of a 3D modeling technique giving promising results in the flapping-wing model is published by Ramamurti et al. [22]. A 3D Drosophila wing is modeled with finite element incompressible flow solver, and the results are compared to experiments conducted by Dickinson et al. [23]. The outcome of the proposed research shows that the thrust and drag forces obtained in the CFD study show good resemblance to experimental results performed by Dickinson et al. [23]. Aono et al. [24] investigated the effect of different Reynolds numbers (Re=134 & Re=6300) on the generation aerodynamic force by the employed flapping-wing structure. An in-house CFD solver is used to the analysis of the hawkmoth wing model. A slightly bigger lift coefficient number is achieved for the Re=6300 condition. On the contrary, the drag coefficient reaches a greater value at the Re=134 regime. Even though in literature, many research studies concentrate on insect-inspired MAV, there are milestone studies proposed on the design and development of avian-based ornithopters. De Croon et al. [25] proposed a study on the design, development of creation steps of DelFly. Mayo et al. [26] introduce a 1 DOF four-bar flapping mechanism activated by a motor. It presents a verification study between experimental PIV results and CFD analysis. It is reported that most of the lift and thrust force augmentation are observed during the downstroke and upstroke phase, respectively. Young et al. [27] investigated the effect of various flapping properties on aerodynamic performance, such as flapping frequency and flapping amplitude using an incompressible Navier Stokes solver. It is concluded that at a constant flapping amplitude, as the flapping frequency increases, the mean vertical produced force and the necessary power for flapping increases. The proposed CFD wing is model is employed for performing 34.5 degrees of flapping amplitude at different frequencies of flapping varying from 1 to 100 Hz. The hover efficiencies gradually increase from 1 to 10 Hz than it shows a plateau characteristic. As the flapping amplitude increases from 10 to 70 degrees at different flapping frequencies changing from 5, 30, and 300 Hz, the hover efficiency shows directly proportional characteristics with frequency and flapping amplitude.

During the flapping motion, MAVs body undergoes aerodynamic and inertial forces. The dynamically moving mechanical parts of the MAV can be attributed to the prior reason of undesired inertial force generation in the opposite direction of the generated lift force. FWMAVs are composed of wing-membrane, flapping-wing mechanism, power sources, and actuator. In recent years, there has been an increasing number of MAV based studies following the development of emerging miniaturized electro-mechanical devices such as light-weight composite parts, motors, sensors, and batteries [28,29]. Due to the highly dynamic behavior of MAV body during flapping motion, small-scale flapping wing vehicles aircraft relatively show large deformations on their body compared to fixed and rotary-wing aircraft. Highly-elastic deformation exhibited during flapping motion influences the aerodynamic performance of the MAVs. However, much of the FWMAV related studies have been performed based on a rigid wing assumption. Thin and flexible features of aerodynamic members of flying creatures have a prominent influence on their aerodynamic performance. They perform striking flight capabilities that are not observed in other flying species, such as high maneuvering, efficient soaring, and high agility characteristics. Several successful studies have already been published to implement and observe the wing-flexion effect on lift and thrust performance [30-31]. Shyy et al. [32] performed the first study to investigate the impact of wing membrane elasticity on fixed-wing MAVs performance by utilizing the FSI (Fluid-structure interaction) method. FSI and experimental studies on flexible wings are performed, and the corresponding results are compared. It is discussed that the MAVs with elastic membrane wings have more adapting capability to stall conditions and performing enhanced agility performance. Cleaver et al. [33]

investigated the effect of flexibility on wing undergoes a sinusoidal heaving motion at a fixed angle of attack. Compared to the rigid wing model proposed in the corresponding study, wing-flexion influences the generated total lift force and enhances the C_L from 1.38 to 2.77. Nakata and Liu [34] performed a complementary FSI analysis for examining the hover mode performance of the Manduca Sexta wing. Besides an integrated computational study consisting of rigid and flexible wing motion is studied, the flapping efficiency is questioned. During the flapping motion, wing deformation occurs owing to inertial and aerodynamic forces and geometrical form of leading-edge changes. The corresponding study reveals that geometrical shape change of leading-edge change due to bending force during flapping motion causes time-lag in the break-down of LEV structures occurring near to the leading edge. This situation leads to the wing-flexion has a prominent influence on boosting up the down-wash in the wake region and total generated lift force production. Also, a notable achievement is reported for wing performing torsional behavior during flapping motion contributes to developing lift force and increases the hovering efficiency. Gopalakrishnan et al. [35] performed a set of analyses to understand the effect of elastic cambering on forwarding flight performance. Different analysis scenarios are created utilizing a rectangular shape undergoing a flapping motion. The corresponding wing models are pre-stressed in the chord-wise and span-wise direction as 8 N/m, 4 N/m, and 2 N/m, and their aerodynamic performances are questioned. It is found that the flapping wing models with high and low pre-stressed in span-wise and chord-wise perform better in aerodynamical force production, respectively.

2.2 Experimental Studies

Experimental studies are conducted to explain the flow structures and force generation mechanisms of flapping motion. The first observation of the flapping wing generates a thrust force that is presented by Knoller [36] and Betz [37]. A NACA wing is forced to perform oscillatory motion as up-stroke and down-stroke, and a time average jet profile is observed in the wake region. Katzmayr et al. [38]

conducted a series of experimental studies to verify the phenomenon presented in [36] and [37]. G189 type Götingen wing section is fixed undergoes a sinusoidally oscillating air stream and measured average thrust. One of the eminent research conducted on FWMAVs is performed by Ellington [39]. He published a series of studies on the aerodynamics of flapping motion for the hovering insect flight, which covers aerodynamical theories, fundamental definitions, and morphological kinematics. In the first study, he examined the quasi-steady aerodynamic mechanisms of the flapping motion. The second and third papers propose detailed information about the morphology of the flapping wing creatures with characteristic wing parameters such as morphological shape, mass distribution [40-41]. In the fourth paper, Ellington compared the theoretical approaches with the available experimental study results for the lift production of hovering flight [42]. The fifth and sixth study published by Ellington presents the theoretical background of the vortex theory and power requirements for flapping-wing systems [43,44]. In 1996, Ellington et al. [45] performed an experimental study and revealed that the LEV is one of the prominent features of the lift force generation mechanism. Before that, LEV mechanism had been known as one of the high-lift mechanisms for the conventional aircraft systems. Based on the quasi-steady state aerodynamic theory, it is impossible to generate a sufficient level of lift force production by flapping motion. In this regard, the leading-edge vortex concept as a high lift mechanism is enlightened with an experimental study [45]. He put forward to the first experimental explanation using by the stereo-photography method to illuminate the high-lift generation mechanisms used by the MAVs. A Manduca Sexta wing model, along with a mechanical system mimicking flapping motion, is utilized for the experiments performed in wind-tunnel. The vortical structures are visualized and observed that high intensity of leading-edge vortex occurs on the down-stroke phase, which contributes as a high-lift force mechanism to the total lift generation.

Currently, experimental studies intensify on characterizing the FWMAVs aerodynamic capability are based on visualizing flow structures around the flapping wing and measuring the generated aerodynamic force utilizing a transducer. To visualize the vorticial structures around the flapping wing PIV technique is used.

PIV is a complementary method that traces the displacement of particles in a fluid under laser light exposure. Lehmann et al. [46] performed an experimental study to demonstrate the effect of a clap-fling mechanism to force augmentation on dynamically scaled fruit fly wings. They employed PIV and force measurements and compared real-time lift force enhancement with time-dependent vorticity structures development. It is concluded that clapping motion develops a modest level of lift force generation. Nonetheless, most of the vortex structures occur at the beginning of the fling motion and generates the majority of the lift force generation.

Muijres et al. [47] conducted a PIV study on larger scale animals. The aerodynamic characteristic of the nectar-feeding bat is experimentally investigated and revealed that they exploit the unsteady aerodynamics mechanism to produce %40 of the total lift force in slow forward flight conditions.

Combes and Daniel [48] investigated how inertial-elastic forces due to the rapid motion of the flapping influences the generated aerodynamic force experimentally. In this regard, a thin Manduca Sexta wing (45µm) is utilized and forced to flap at a realistic wing-beat frequency. To show the aero-inertial effect causes bending on wing structure, an experimental study is conducted in air and helium medium. Combes and Daniel [48] revealed that %85 percent of density reduction has minimal influence on bending occurrence on the flapping wing. The majority of the bending forces stem from the inertial loads of the wing structure.

In many studies, the total aerodynamic force and moment characterization of a corresponding system are done by 6-axis force measurement. Verification of the numerical and theoretical approaches with experimental results have crucial importance for generating applicable parametric and time-saving methods for further MAV studies. Most of the studies carried out to measure lift and drag forces utilize traditional test stands. Sane et al. [49] implemented the force sensor to a wing and measured the aerodynamic forces. Some MAV models are not suitable for the direct implementation of the force sensor. A strain-gage implemented on cantilever beam design is used to calculate the generated lift force by the corresponding MAV body. The reliability of this method is highly dependent on the material properties of the utilized beam, and the experiments should be run in a conditioned environment to obtain reliable results [50-51].

CHAPTER 3

METHODOLOGY

This section presents the methodological background for design and verification studies associated with the inertial and aerodynamic characterization of the introduced flapping wing mechanism. The proposed methods are constructed by employing experimental, theoretical, and numerical approaches. Firstly, the geometrical and kinematical properties of the utilized mechanism are proposed. Then the design steps of the test-platform engineered for the conducted flapping experiments that include CAD model development and modal characterization studies are presented. An inertial characterization is performed for the flapping wing mechanism to understand the standalone effect of the produced inertial forces on the aerodynamic forces. In the inertial characterization study, first, a sensor calibration study is performed, then the inertial forces generated by the flapping mechanism without the wing membrane is investigated by experimental, theoretical, and numerical approach. Lastly, an aerodynamic characterization study is employed for the utilized flapping wing mechanism. An experimental flapping test is conducted, including the wing membrane. The test results are compared to the fluid-structure interaction analysis model that is developed for the corresponding flapping-wing mechanism.

3.1 Geometry and the Flapping Model

In this study, a generic flapping wing mechanism with a gear, rod, and crank is utilized to demonstrate the flapping motion. The main actuation is generated by 1 gr electric motor, and the rotary motion is transformed into the flapping motion through three spur gears, two pinion gears, and two linkages. Inherently, the utilized flapping wing mechanism offers a tandem flight with four wings. However, in this study, the number of wings is reduced, and the proposed mechanism is opted to be used as a two-winged flapping mechanism for simplicity purposes. The frontal view of the utilized mechanism, along with the major properties of the gears are given in Figure 3.1.

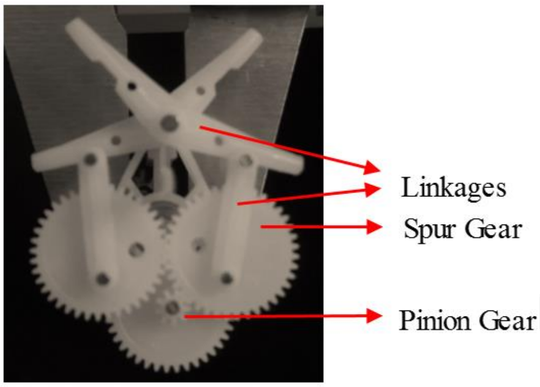

a

	Modulus	Number Of Teeth
Pinion Gear	0.3	9
Spur Gear		40

b

Figure 3.1: The utilized flapping mechanism a) Front view of the mechanism b) Properties of the spur and pinion gear

The CAD model and characteristic dimensions of major parts of the utilized mechanism is given in Figure 3.2 and Figure 3.3, respectively.

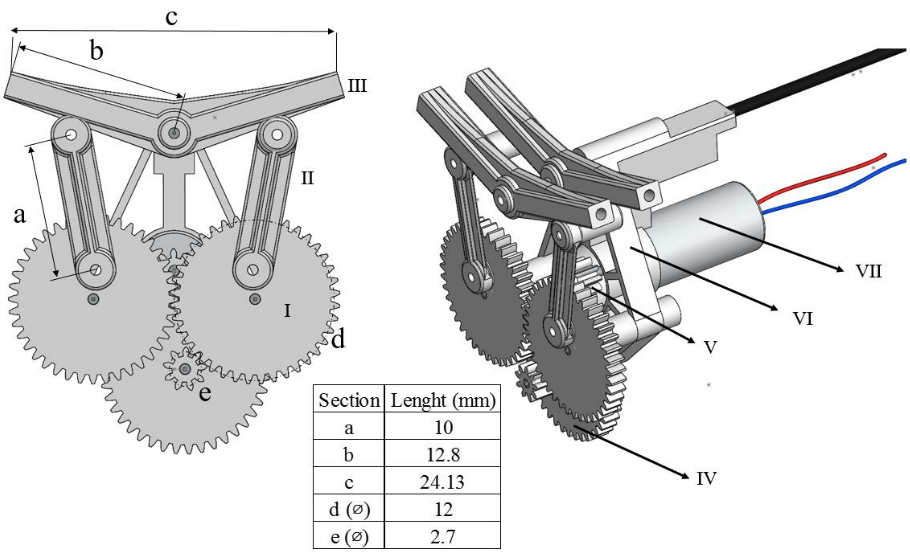

Section	Lenght (mm)
a	10
b	12.8
c	24.13
d (⌀)	12
e (⌀)	2.7

Figure 3.2: Utilized flapping wing mechanism system with major dimensions

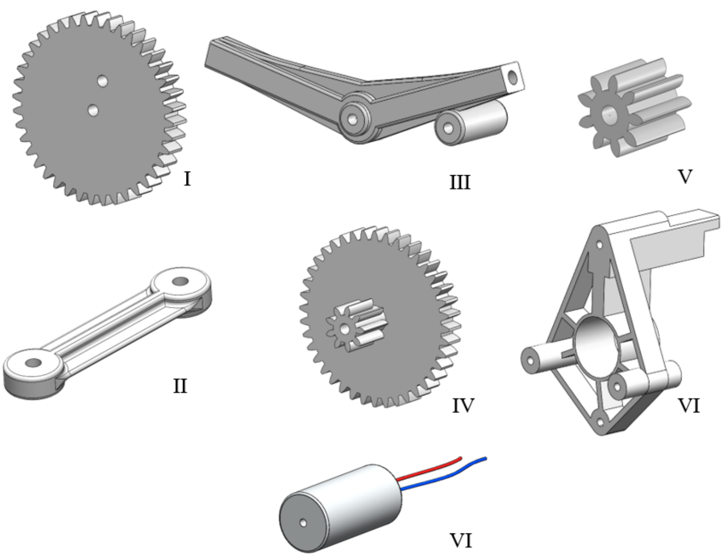

Figure 3.3: Visual representation of the proposed system

The utmost and least possible angular positions reached by part-III, which determines the achieved flapping angles, are given in Figure 3.4. The utilized mechanism offers 30 degrees of flapping angle between 20° and 50° to the horizontal axis.

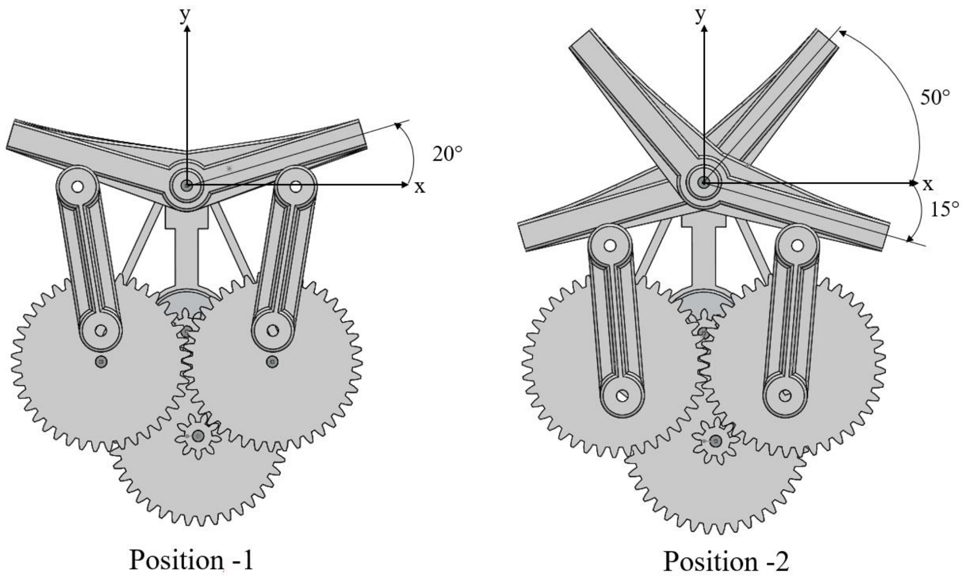

Figure 3.4: Upper and lower flapping positions of the proposed mechanism

3.2 Test Platform Design

In this section, an experimentally purposed test-platform designed for a flapping-wing application is presented. Flapping-wing mechanisms are mechanisms that include dynamically moving parts, such as gears, linkages, and connection elements performing synchronized perpetual motion throughout the flapping event. This situation causes the test stand is subjected to dynamical loading during the experiment. Therefore, a test stand exhibits robust characteristics under a vibrational load that is desired to design. In this study, the upper flapping frequency of the designed test is determined as 23 Hz. Within this framework, a CAD model is developed, and modal characterization studies are performed for the desired test-stand. The developed CAD model of the flapping test-stand is given in Figure 3.5.

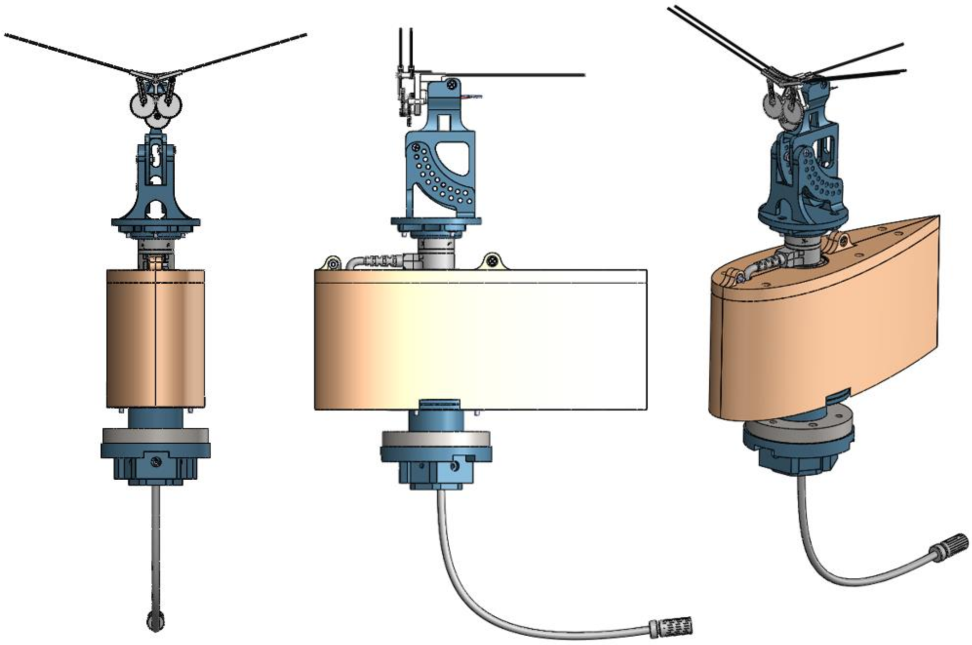

a b c

Figure 3.5: Developed Flapping test stand a) Front view b) Side view c) Isometric view

The cutaway and exploded view of the proposed test-stand is given in Figure 3.7. An angle-adjustable bracket is developed for arranging a specific angle of attack with five increments of angles. In this study, a 6 mm diameter with an 11 mm length electric motor is utilized for driving the flapping mechanism. The electric motor is the common interception part where the flapping wing mechanism and test-stand are attached. Therefore, the force developed by the flapping wing mechanism is directly transferred to the test-stand through the body of the electrical motor. In this manner, the electric motor – test stand connection should provide a robust connection, and the movement of the motor is fully-restricted. The diameter of the motor mounting hole is dimensioned the same with motor diameter. This situation leads to a tight fit connection between the motor and its case. Besides, the mounting case is pre-stressed with a preloaded M2 bolted joint for ensuring to restrict the motor movement in each its translational and rotational axis as it is given in Figure 3.6.

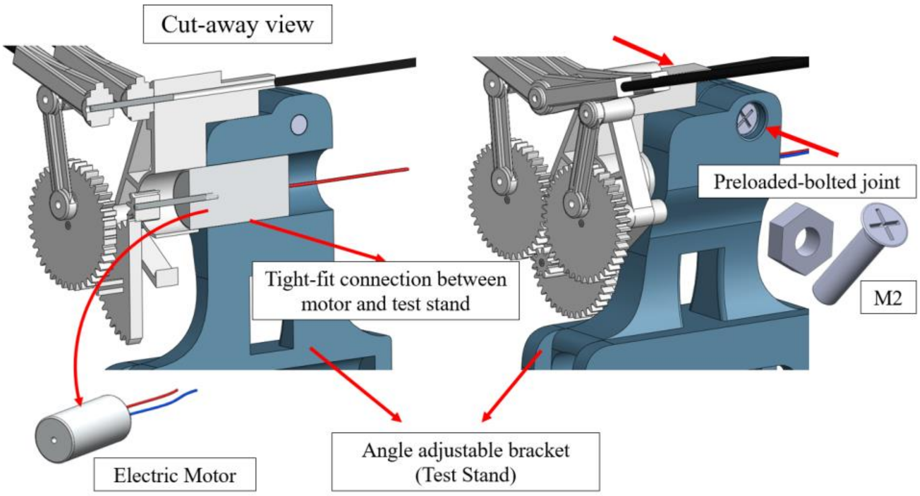

Figure 3.6: Test stand - motor connection

During the flapping test, a preserved flow characteristic is desired around the flapping wing for ensuring the accuracy of the performed test results. The perturbed flow regime may influence the flow around the wing and cause undesired aerodynamic force results. In this fashion, it is aimed that the potential undesired vortex-generating forms are hidden constructively, such as bulge, slotted, irregular forms, and cabling elements. The slotted part (Figure 3.7, Part 5) is cased with a NACA0030 airfoil profile (Figure 3.7, Part 7) for preventing the generation of undesired vortex structures by the part 5 given in Figure 3.7.

The primary focus of the developed test-stand is to acquire the real-time aerodynamic force and torque data during the flapping wing test. The ATINANO 17 (Figure 3.7, Part 4) six-axis F/T (Force/Torque) sensor is utilized. Since the experimental test setup is modified to work in a wind tunnel, the cabling elements of the used sensor is hidden and passed through inside of the slotted part (Figure 3.7, Part 5) to preserve the flow characteristic around the wing.

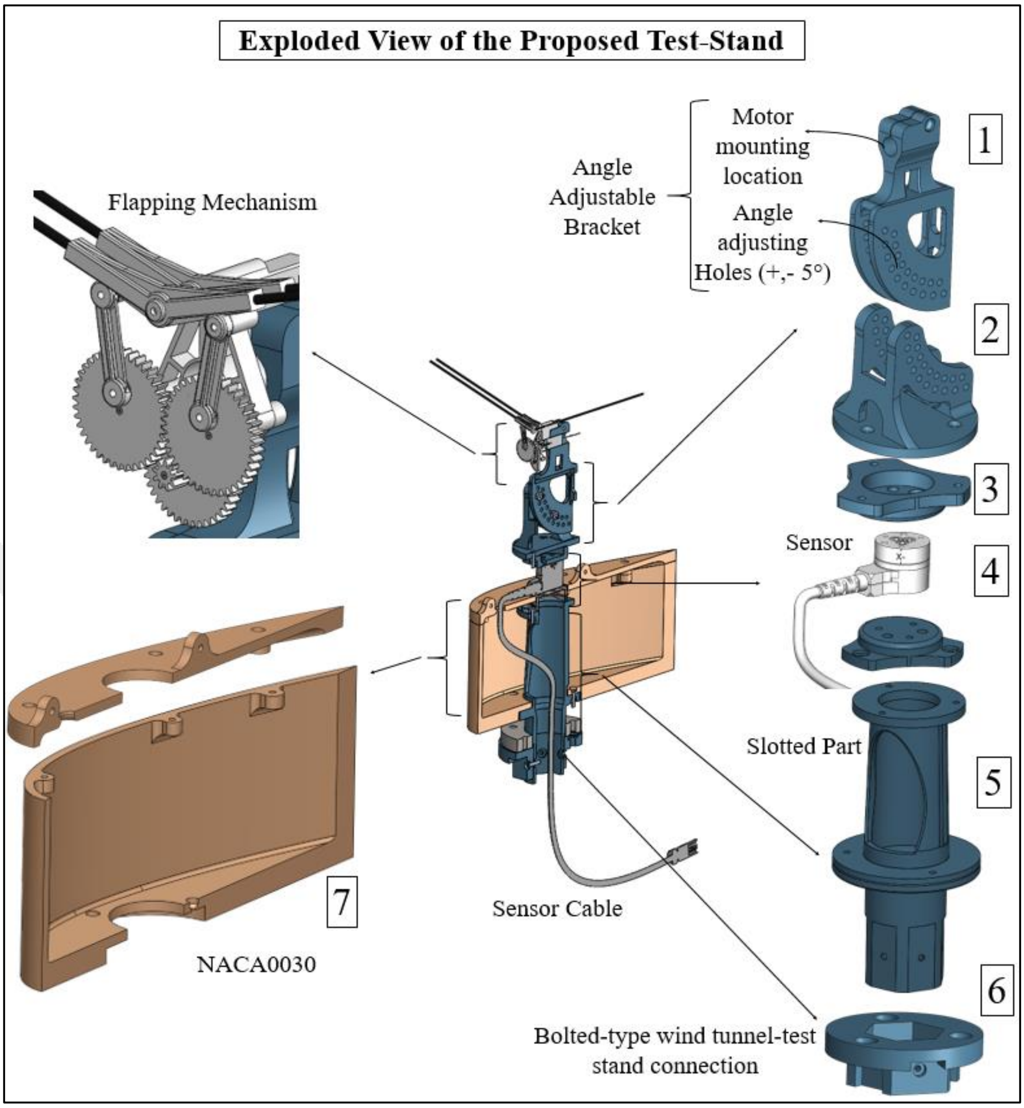

Figure 3.7: The exploded view of the developed test stand

A modal analysis is performed to understand the frequency response of the developed test platform. The meshed view of the proposed test-setup is given in Figure 3.8. The FEA model is simplified, and the mass of the attached mechanism is represented as a point mass defined from its center of gravity location. The number of assigned nodes and cell types are given in Table 3-1. The elastic modulus of the ABS material is defined as 3GP with 0.3 Poisson Ratio [52].

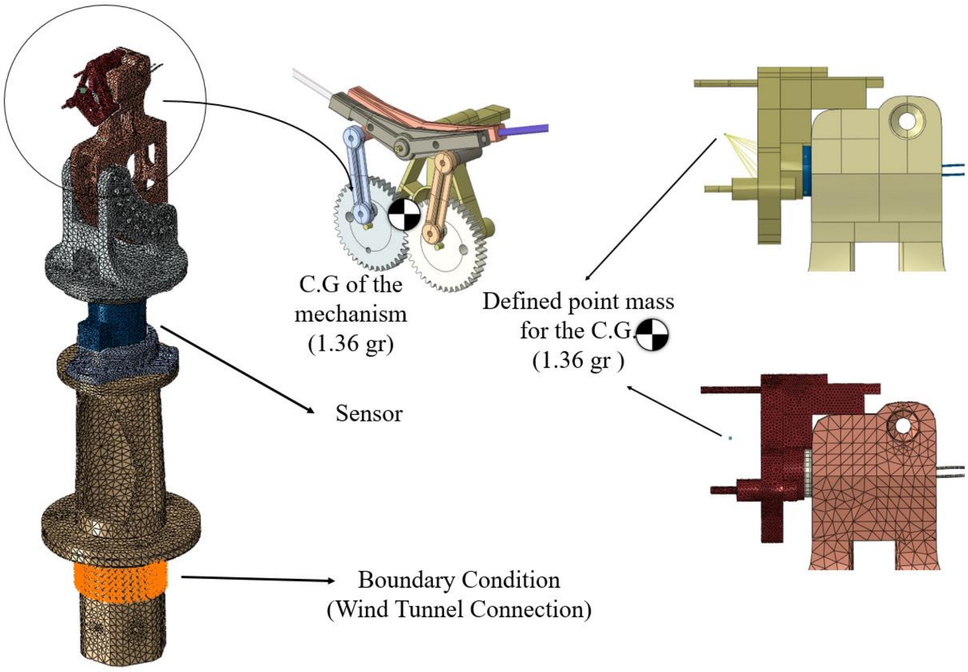

Figure 3.8: Modal analysis model created for the proposed Flapping mechanism and test stand

Table 3-1: The assigned cell properties for the modal analysis

Cell Name	*Cell Type*	*Number of Nodes*
linear hexahedral	C3D8	5148
linear tetrahedral	C3D4	284995
quadratic tetrahedral	C3D10	26445
Total Node Number	109973	
Total Element Number	316588	

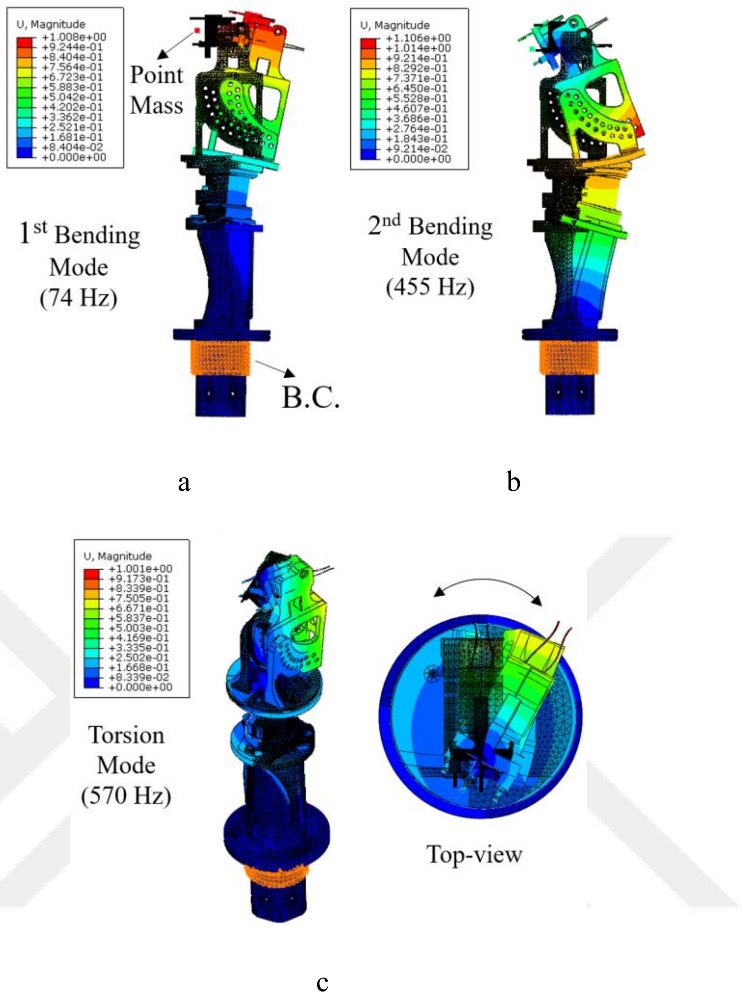

Figure 3.9: Modal analysis result of the developed test-stand

According to the modal analysis result given in Figure 3.9, the first and second bending mode of the proposed structure is found as 74 Hz, 455 Hz respectively. The torsion mode of the structure given in Figure 3.9 c as 570 Hz. Since the natural modes of the structure higher than the operational frequency planned for the flapping test, the corresponding structure is assumed as safe to use.

The corresponding parts are manufactured with the additive manufacturing technique. The produced test stand is given in Figure 3.10, and the assembled view of the developed test stand in the wind tunnel is given in Figure 3.11.

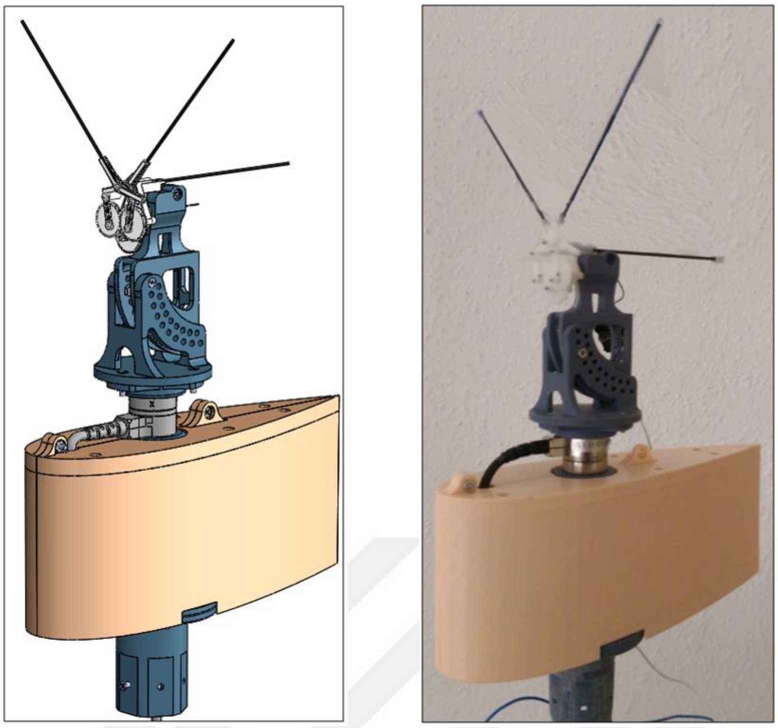

a b

Figure 3.10: The developed test stand a) 3D Model b) Fabricated

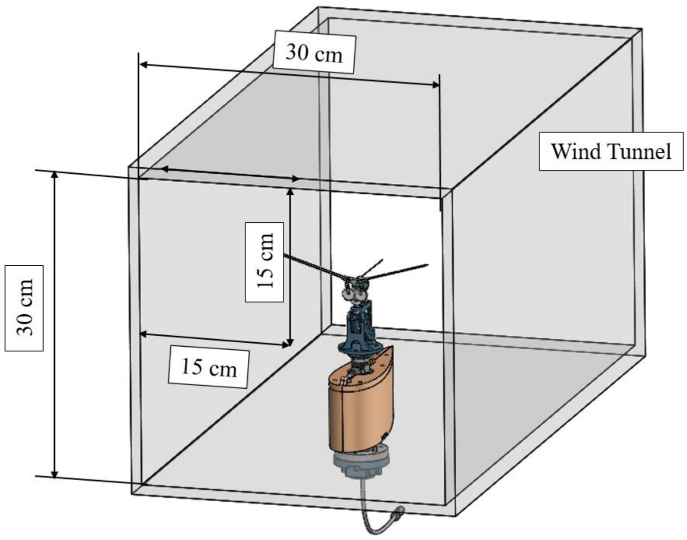

Figure 3.11: The ISO View of the developed test-stand in the wind tunnel

3.3 Inertial Characterization of the Flapping Wing Mechanism

During flapping motion, two-types of forces act on the flapping wing as inertial forces and aerodynamic forces. The total lift force acting on the whole aircraft body is the summation of time-dependent vectorial inertial and aerodynamic forces. The inertial forces are defined as the standalone inertial effect that is generated by the dynamically moving parts of the flapping mechanism. The inertial forces act as an opposing force to the aerodynamic force and attenuate the total generated aerodynamic force, especially for the systems performing non-symmetric flapping motion to the horizontal axis. For the flapping test performed in air, the force sensor measures the total of the inertial and aerodynamic forces. In this framework, characterizing inertial force has a pivotal role in understanding the pure aerodynamic force capability of the utilized flapping system.

In order to measure the pure inertial forces created by the proposed flapping mechanism, the wing membrane is detached from the flapping mechanism, and a flapping experiment without a wing membrane is conducted (Figure 3.12). Then the numerical and theoretical approaches are proposed to verify inertial forces obtained in the performed flapping test.

Figure 3.12: Flapping wing mechanism without the wing skin

Throughout the test-theory and analysis process, the flapping frequency is employed based on 22.8 Hz. Force and Torque values are measured by using 6-axis sensor ATI Nano17 with ±17 N sensing range in the z-direction (lift direction), ±12 N sensing ranges in x and y-direction. Labview program is utilized for recording purposes. The experimental test setup is given in Figure 3.13.

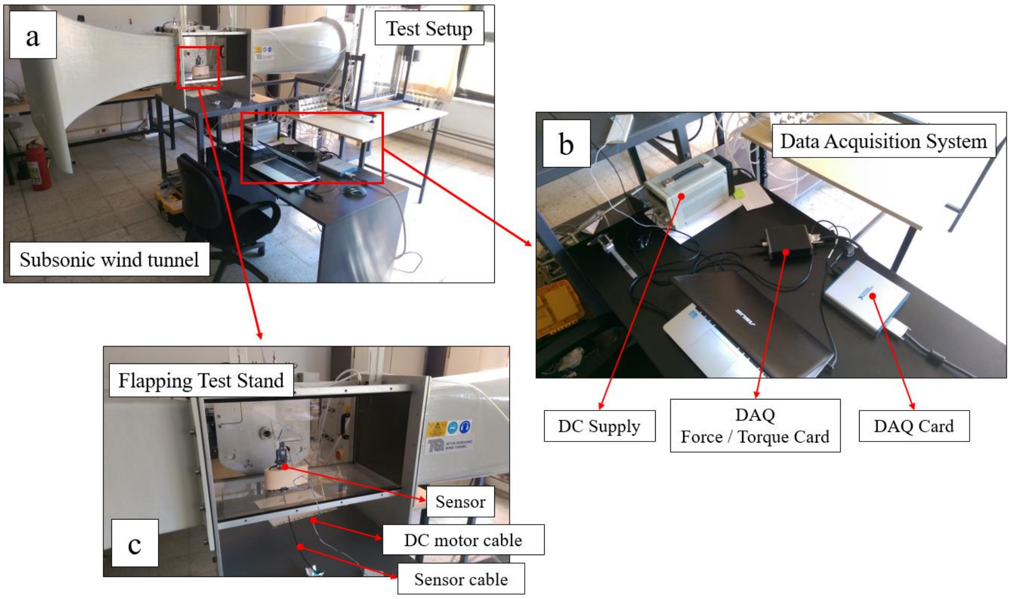

Figure 3.13: Experimental test setup a) Test setup b) Data acquisition system c) Flapping test stand

Following the initial hands-on experience gained in the force sensor, it is understood that the utilized force sensor produces a significant amount of measurement error due to a lack of calibration. In this regard, a distinct, simple test case is designed to calibrate the force sensor by neglecting the flapping mechanism and implementing a simple carbon rod. The rigors regarding the force sensor are demonstrated in further sections by performing real-time data acquisition test.

In the previous modal analysis section, it is indicated that the developed test stand is designed to be able to perform under flapping frequency to minimize the occurrence of residual force during the real-time test. However, the rotating parts inside of the gearbox set of the utilized by the flapping mechanism reaches far beyond the flapping wing speed. As a consequence, the developed test stand is excited by the high-frequency rotating elements as (40:9) x (40:9) times higher than flapping-wing frequency. This situation leads to the excitement of the proposed test-stand to its natural frequency. In this regard, a low pass filter is applied to the test data, and results are reported. A 3-step methodology followed in this study regarding the validation of test, theory, and analysis study is given in Figure 3.14. To keep the production costs low and obtaining a slim looking test-stand that prevents behavior of the flow structures minimally during wind tunnel experiments, any thickening studies regarding increase the first bending mode study have not been employed.

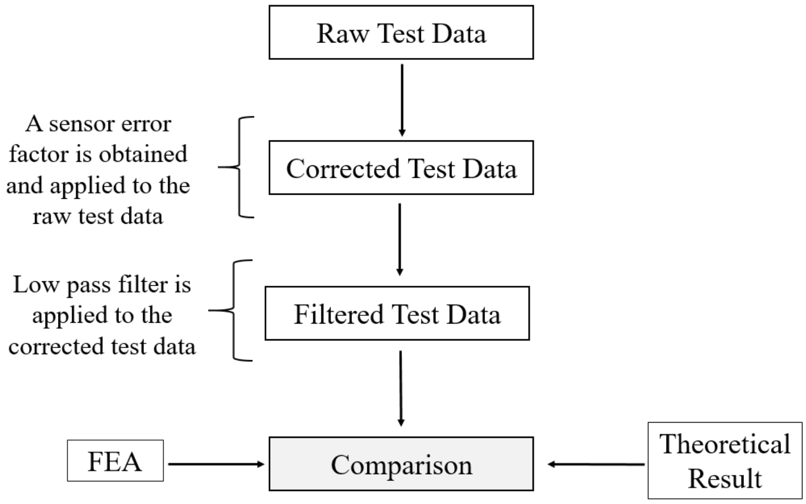

Figure 3.14: Methodology followed for test, theory and, analysis validation of the inertial characterization

3.3.1 Dynamic Calibration of the Utilized Sensor and Flapping Test (Without Wing Membrane)

This section presents the dynamic calibration session applied to the utilized force sensor. The problem regarding the outcome of the sensor data is demonstrated on a simple test, and a solution proposal for calibrating the utilized sensor to overcome the arisen sensor error is mentioned. In order to verify the acquired sensor data, dummy masses are placed on the sensor, and data outputs are checked as given in Figure 3.15.

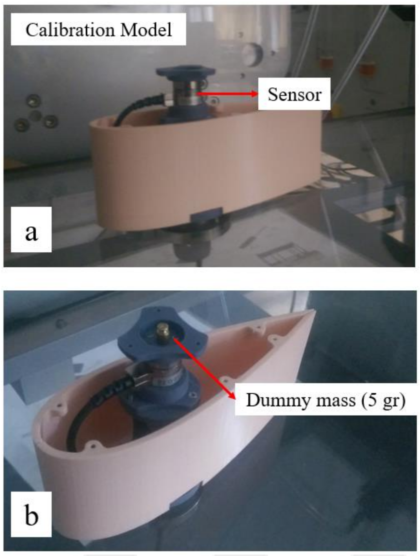

Figure 3.15: Sensor calibration model a) Simplified test stand for Calibration b) 5 gr Dummy mass put on sensor

After a simple demonstration conducted with dummy-masses, it is concluded that the utilized force sensor is saturated, and it measures distinct values for the same mass put on the different pin-point locations on the sensor surface as it is given in Figure 3.16.

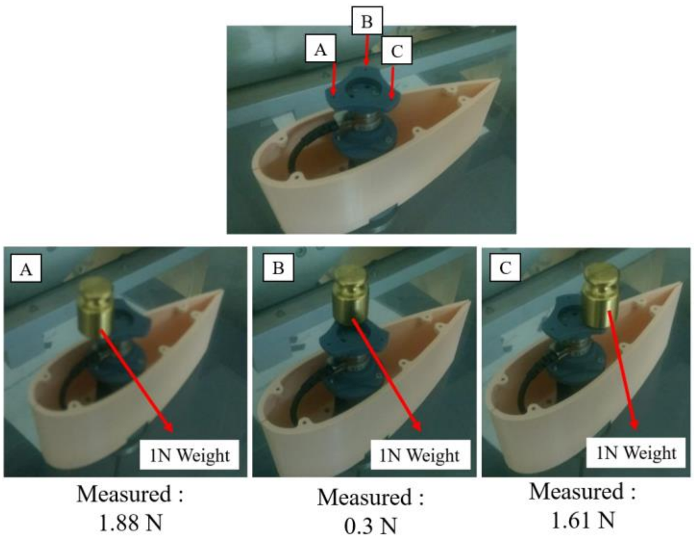

Figure 3.16: Dummy mass placed on different locations on the sensor a) Dummy mass put on the point A and measured value b) Dummy mass put on the point B measured value c) Dummy mass put on the point C measured value

As seen in Figure 3.16, the pinpoint location of the force applied is the critical point of obtaining an error function for the utilized force sensor. Thus, the force sensor shows case-dependent characteristics depending on where force is exerted on its surface. Therefore, it is concluded that the utilized force sensor outputs a force data concerning the center of gravity of any system placed on the force sensor.

For the dynamic calibration session, a simplified test model is offered by eliminating the gears of the corresponding flapping wing mechanism, as it is given in Figure 3.17. A 6.3 10^{-6} kg mass carbon rod with 0.0032 m length of the rod is attached to the spur gear head, and the inertial effect of the carbon rod at a specific rpm is investigated as a loaded and unloaded case (Figure 3.18).

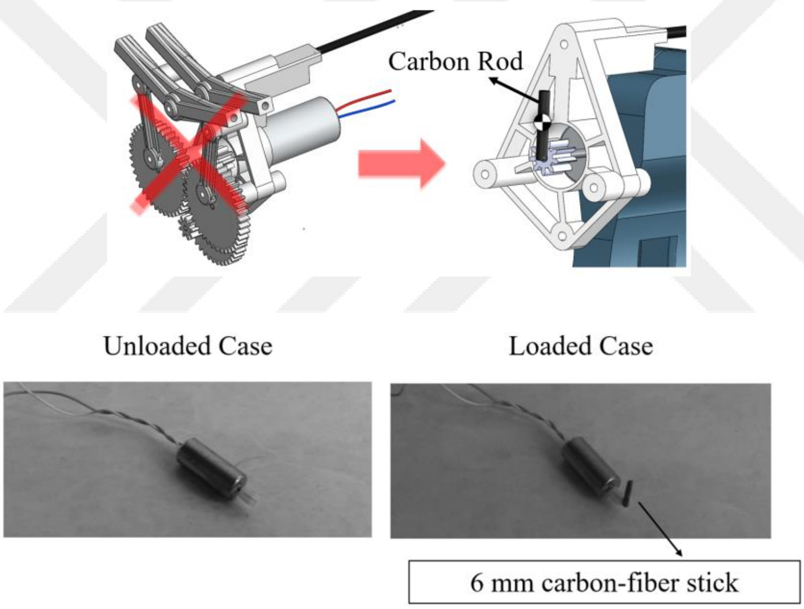

Figure 3.17 The simplified test setup

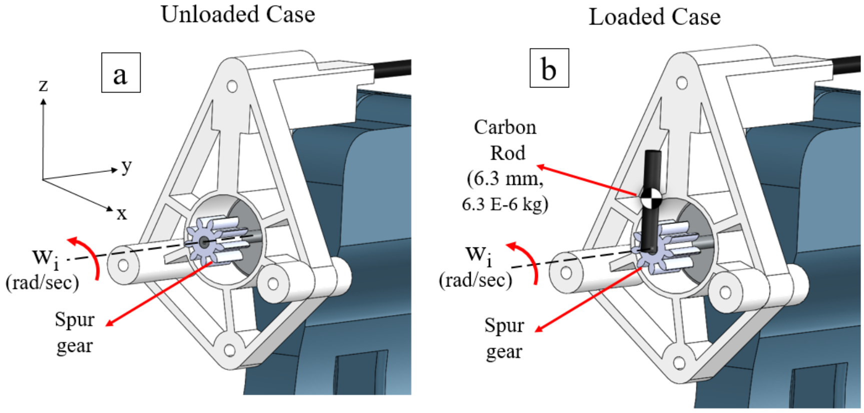

c

i	Voltage
1	1
2	1.5
3	2
4	2.5
5	3
6	3.5
7	4

Figure 3.18: Simplified test model a) Unloaded case b) Loaded case c) Applied voltage

The FFT test result for the whole voltage scenarios is given in Figure 3.19.

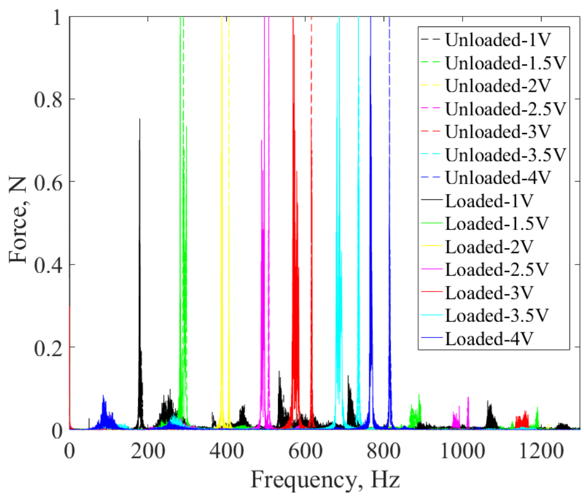

Figure 3.19: FFT results of the test scenarios

The FFT results of each voltage case are pin-pointed and given as tabulated form in Table 3-2.

Table 3-2: Pin-pointed FFT values for each test case

i	*Voltage (V)*	*Unloaded Case (Hz)*	*Loaded Case (Hz)*
1	1	183	179
2	1.5	290	281.4
3	2	406	388.6
4	2.5	507	495
5	3	615.9	572
6	3.5	735.5	687
7	4	814.6	766.4

A theoretical approach is used and compared to the test result to find a sensor error factor. It is considered that the force difference between unloaded and loaded cases (Figure 3.20) gives the pure inertial force generated by the carbon-rod. Also, a reliability study for the performed theoretical approach is conducted with a dynamic FEA analysis for the 1 V case (179 Hz, Figure 3.20, Figure 3.21).

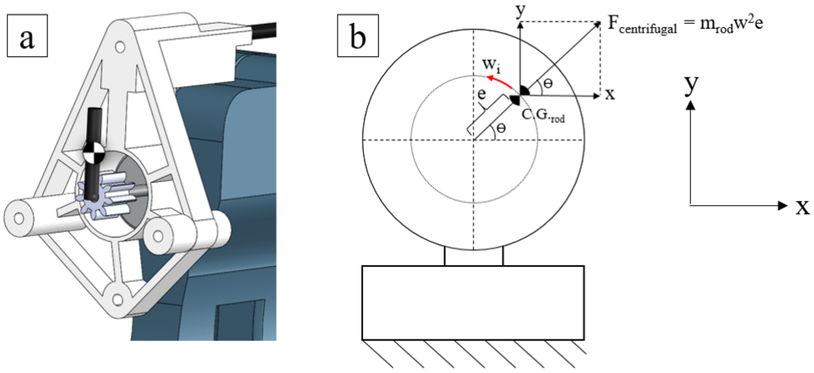

c

i	Voltage	Frequency (Hz)	wi (rad/sec)
1	1	179	1124.69
2	1.5	281.4	1768.09
3	2	388.6	2441.65
4	2.5	495	3110.18
5	3	572	3593.98
6	3.5	687	4316.55
7	4	766.4	4815.43

mrod (kg)	2e (mm)
6.30E-06	6.39mm

Figure 3.20: Theoretical model applied for different cases a) CAD model b) Theoretical model c) Conducted different test scenarios

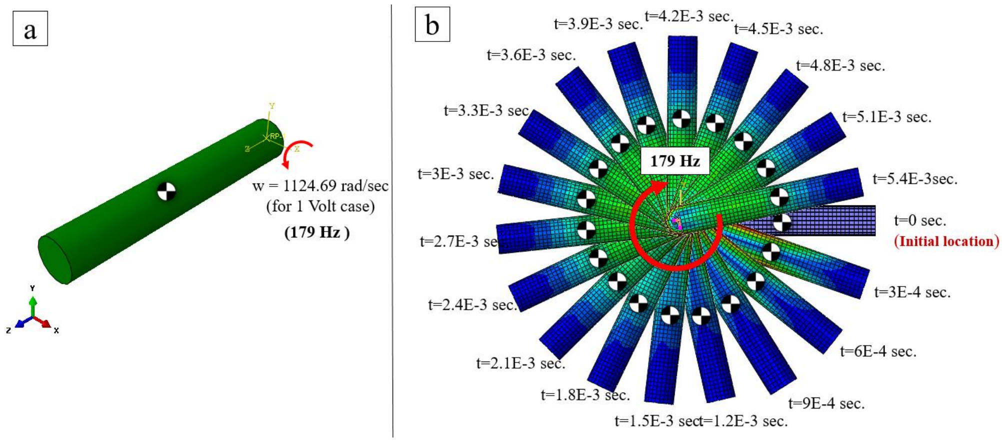

Figure 3.21: The validation of the inertial force created by the implemented carbon rod a) FEA model b) Time-dependent angular locations of the part during the Rotation

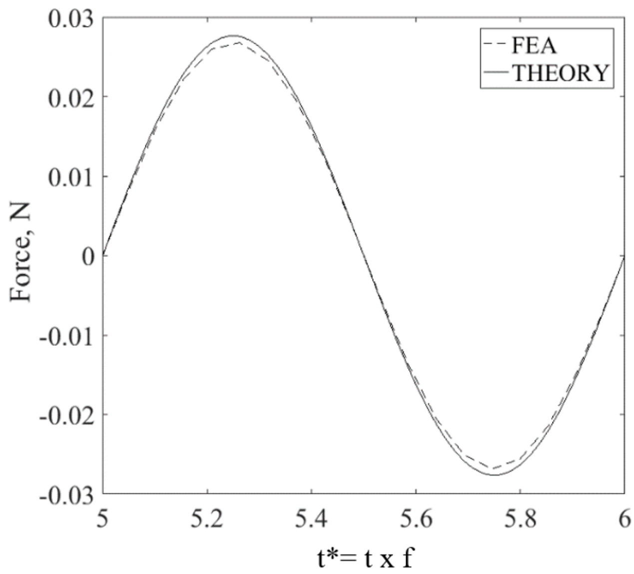

Figure 3.22: FEA-Theory comparison for 1V case (179 Hz)

As it can be seen from Figure 3.22, the FEA and theoretical results show great agreement for the vertical force results (Figure 3.20– y-direction). In this manner, the expressed theoretical formulation is governed in further sections to find out the error margin created by the utilized sensor. The error generated by the sensor is found out and attained as an amplification factor for the measured force data. However, since the flapping test is performed at approximately 23Hz (Flapping wing frequency occurs at 3V), only the error function for the corresponding voltage case is shared

(3V case). The force difference occurs between the loaded and unloaded cases (Figure 3.17) gives the pure inertial effect of the attached carbon-rod. By comparing the measured force difference between both cases and theoretical inertial force value, an amplification ratio is obtained for the corresponding voltage case and applied to the raw data. The amplification ratio attained for the 3V case is found out as 1.93 and given in Table 3-3.

Table 3-3: Amplification ratio obtained for 3V Case

3 VOLT CASE (572 Hz)					
	Loaded Case*, N	Unloaded Case*,N	ΔF_{3_Volt}, N (*)- (*)	Theoretical Result, N	Amplification Ratio (Test/Theory)
Measured Max. Force (N)	1.08	0.538	0.542	0.28	1.93

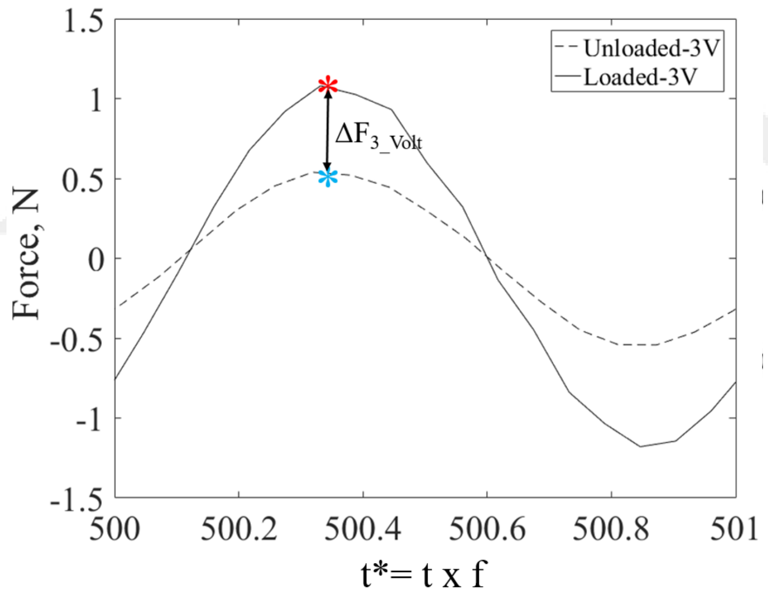

3.3.2 Rigid-Body Dynamics Calculations

In this section, it is desired to find the inertial forces generated by mechanical parts of the utilized flapping mechanism by utilizing a theoretical approach. A theoretical study employing rigid-body formulations is presented for the verification of the dynamic FEA model and experimental results. The characteristic properties of the mechanical parts involved in the inertial force calculations belong to the flapping mechanism are given in Table 3-4.

Table 3-4: Characteristic properties of the utilized flapping mechanism for the inertial calculation

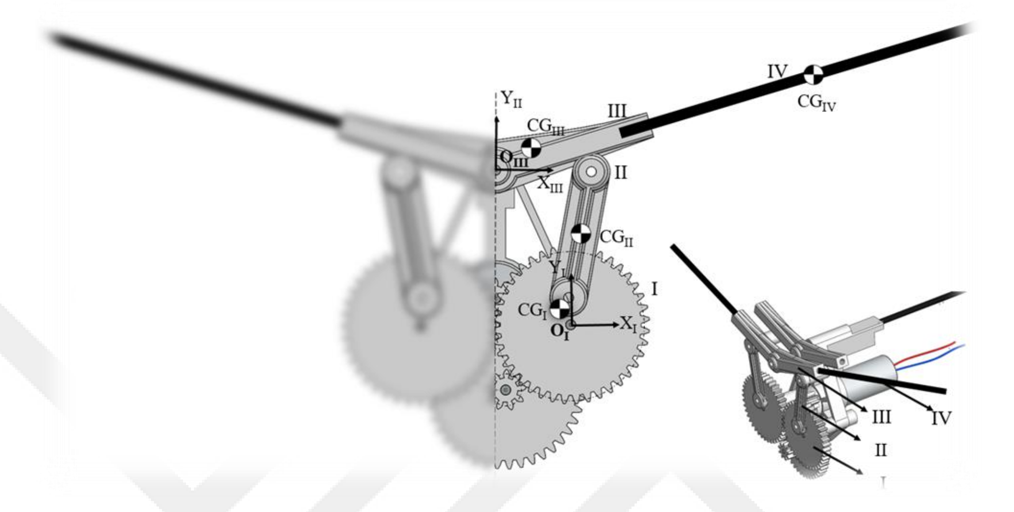

Part	Quantity	Mass, kg	Rotation Axis	The radius of rotation, m
I	2	2.31e-4	O_I	2.45e-4
II	2	4.02e-5	O_I	Elliptical (Various)
III	2	2.25e-4	O_{III}	2.4e-3
IV	2	7.66e-5	O_{III}	3.37e-2

When a body undergoes a rotational motion around a specific axis or follows an arbitrary trajectory, it creates an inertial force around its rotation axis. In this framework, the rigid body dynamics calculations are conducted for the depicted parts in Table 3-4.

The instantaneous position of an arbitrary particle in planar motion and the unit vectors that occur through the planar motion are depicted as radial (i_r), and transverse (i_θ) components, as illustrated in Figure 3.23. The position of an arbitrary particle moving on a coordinate system depicted in Figure 3.23 described by Pytel et al. [53] with a radius to the origin is $r=ri_r$ is found as;

$$i_{\mathrm{r}} = \cos(\Theta_i) + \sin(\Theta_j) \tag{1}$$

Derivative of i_{r} with respect to time,

$$\dot{i_{\mathrm{r}}} = \dot{\theta}(-sin(\Theta_i) + \cos(\Theta_j)) \tag{2}$$

The transverse unit vector is defined as;

$$i_\theta = -\sin(\Theta_i) + \cos(\Theta_j) \tag{3}$$

Derivative of i_θ with respect to time,

$$\dot{i_\theta} = \dot{\theta}(-\cos(\Theta_i) - \sin(\Theta_j)) \tag{4}$$

Hence,

$$\dot{i_\theta} = -\dot{\theta} i_{\mathrm{r}} \ (5)\ ,\ \ i_{\mathrm{r}} = \dot{\theta} i_\theta \ (6)$$

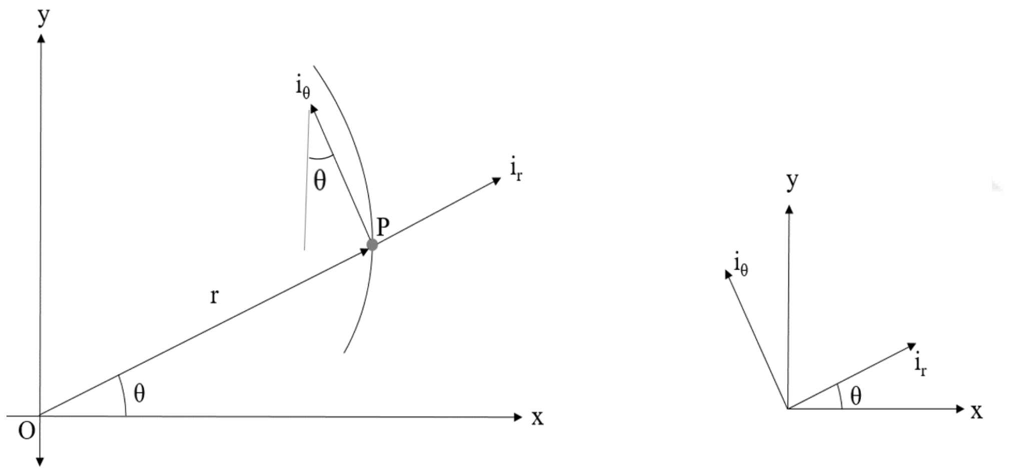

Figure 3.23: Arbitrary motion of a particle (Re-illustrated from [53])

The velocity component in the polar coordinate system given in is found as [54];

$$v = \frac{dr}{d\mathrm{t}} = \frac{dr}{dt}\ i_{\mathrm{r}} + r\frac{di_{\mathrm{r}}}{dt} \tag{7}$$

Where $r = \ i_{\mathrm{r}}$

using the chain rule;

$$v = \frac{dr}{dt}\ i_{\mathrm{r}} + r\frac{d\theta}{dt}\ \frac{di_{\mathrm{r}}}{d\theta} \tag{8}$$

$$v = \dot{r}i_r + r\dot{\theta}i_\theta \qquad (9)$$

The acceleration term is obtained by taking the derivative with respect to time of the velocity term given in (8)

$$a = \frac{dv}{dt} = \ddot{r}\, i_{\mathrm{r}} + \dot{r}\frac{di_{\mathrm{r}}}{dt} + \dot{r}\dot{\theta}i_\theta + r\ddot{\theta}i_\theta + r\dot{\theta}\frac{di_\theta}{dt} \qquad (10)$$

Here, $\frac{di_{\mathrm{r}}}{dt}$ is defined as $\frac{di_{\mathrm{r}}}{dt} = \dot{\theta}i_\theta$ (5) and $\frac{di_\theta}{dt}$ (6) is defined as $\frac{di_\theta}{dt} = -\dot{\theta}i_r$

The radial and transverse components of the velocity and acceleration is found as;

$$v_{\mathrm{r}} = \dot{r}\ (11),\ \ v_\theta = r\dot{\theta}\ \ (12)$$

$$a_{\mathrm{r}} = \ddot{r} - r\dot{\theta}^2\ (13),\ \ a_\theta = r\ddot{\theta} + 2\dot{r}\dot{\theta}\ \ (14)$$

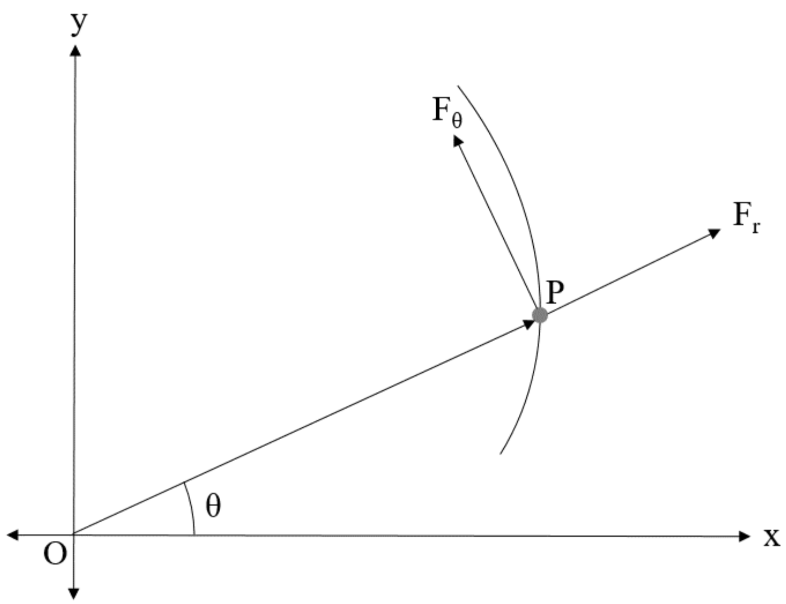

Figure 3.24 Exerted forces on a particle during planar motion

Utilizing the (13) and (14), the exerted forces on a particle during planar motion given in Figure 3.24 can be found as;

$$F_{\mathrm{r}} = ma_{\mathrm{r}} \qquad (15)$$

$$F_r = m(\frac{d^2r}{dt^2} + r(\frac{d\theta}{dt})^2) \qquad (16)$$

$$F_\theta = ma_\theta \qquad (17)$$

$$F_\theta = m(\frac{d^2\theta}{dt^2} + 2\frac{dr}{dt}\frac{d\theta}{dt}) \quad (18)$$

Herein, the $\frac{d^2r}{dt^2}$ and $r(\frac{d\theta}{dt})^2$ in (16) represent the acceleration toward/away from the origin and centripetal term, respectively. In (18), $\frac{d^2\theta}{dt^2}$ and $2\frac{dr}{dt}\frac{d\theta}{dt}$ terms represent the angular acceleration around the origin and the Coriolis acceleration term.

According to the equations that are derived for the planarly moving part, two types of forces exerted on a particle in its corresponding radial and transverse direction, as it is given in Figure 3.25. In this study, for the further sections, the forces exerted on radial, and transverse axes are called centrifugal force and tangential force for simplicity.

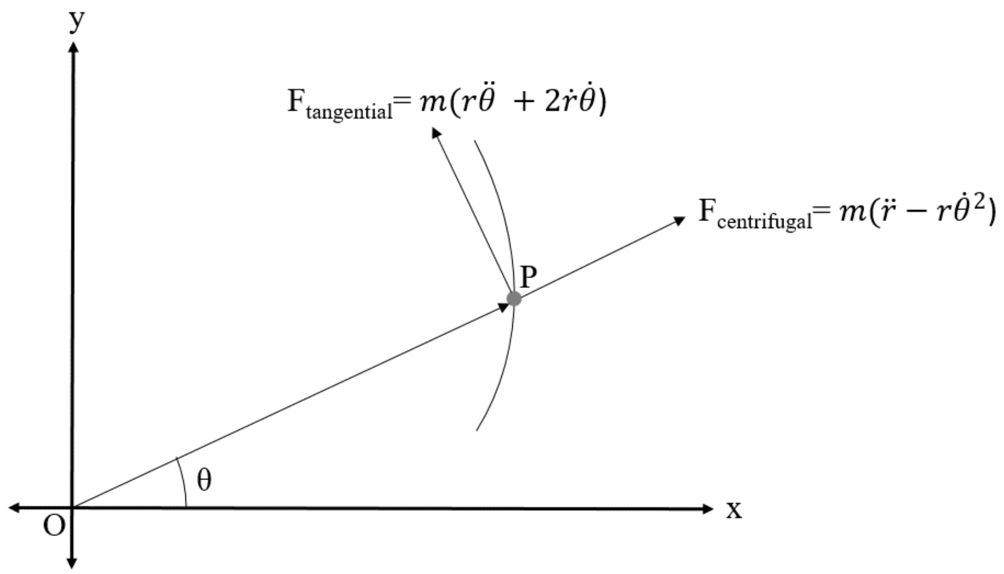

Figure 3.25: Open form of the forces acting on the particle

3.3.3 Dynamic Finite Element Analysis Model

A dynamic FEA study is conducted for the 22.8 Hz flapping case to validate the theoretical and experimental results. The created FEA model is given in Figure 3.26.

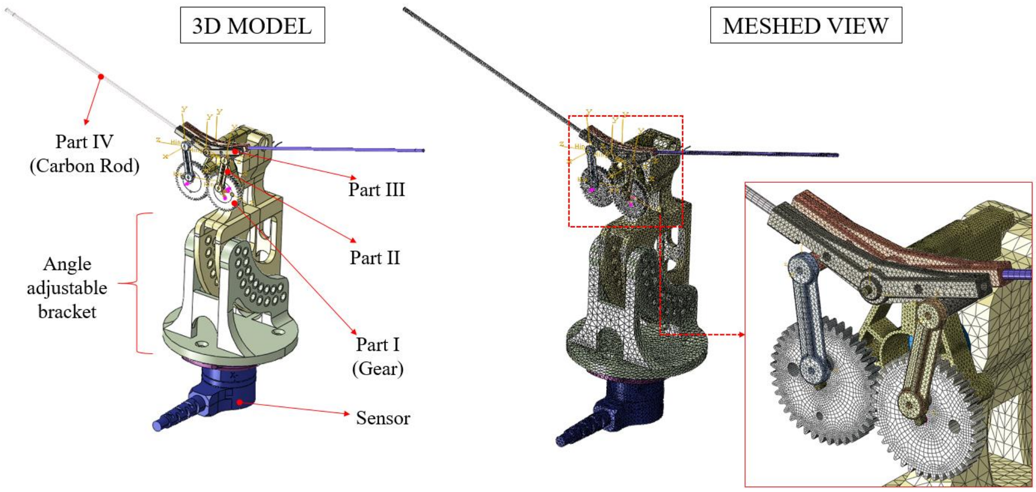

Figure 3.26: Dynamic FEA model

The defined materials and their properties in the dynamic FEA model are given in Figure 3.27 and Table 3-5, respectively.

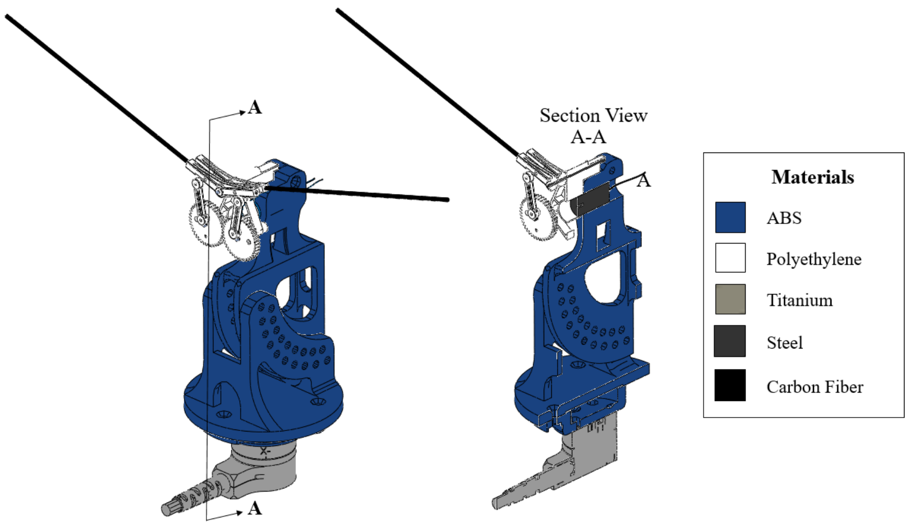

Figure 3.27: Defined materials in FEA models

Table 3-5: Material properties defined in the dynamic FEA model

Material Properties (* Empirically Obtained)			
Material	Density (gr/cm^3)	Elastic Modulus (GPa)	Poisson's Ratio
ABS	0.7 *	2.5	0.3
Polyethylene (Plastic Parts)	1.25 *	2	0.3
Titanium (Sensor Material)	3.3*	300	0.3
Steel	7.2	210	0.3
Carbon Fiber (Linear Assumption)	1.45*	145	0.35

The loads and boundary conditions applied to the created dynamic FEA model is given in Figure 3.28. A rotational load defined to the gears and the movement of the model is fixed from the sensor attachment point.

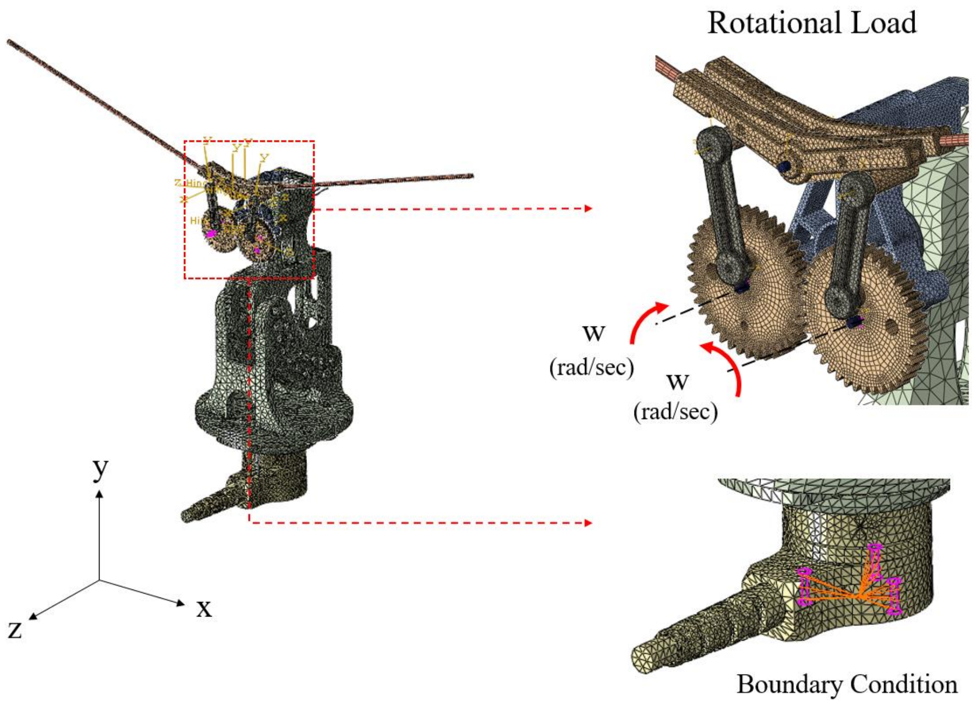

Figure 3.28: Loads and boundary conditions defined in the FEA model

3.4 Aerodynamic Characterization

3.4.1 Flapping Experiment

In this section, a flapping test with a wing membrane is performed to characterize the vertical forces generated by the flapping motion. An elliptical planform is selected for the wing skin coverage for simplicity purposes. The length of the leading edge rod is specified as 7 centimeters, which makes leading-edge reach to its maximum value to satisfy to be able to perform under the restrictions of MAV definition (Span < 15 cm) [1]. A freezer bag nylon material with 10 microns thickness material is utilized. The blueprint of the elliptical planform is overlaid on nylon material and fixed. The edge of the wing planform is painted with a marker and cut-out from its boundaries. The final wing skin product is detached from the nylon layout and attached to three different sections of the corresponding mechanism. The wing skin and final product are given in Figure 3.29.

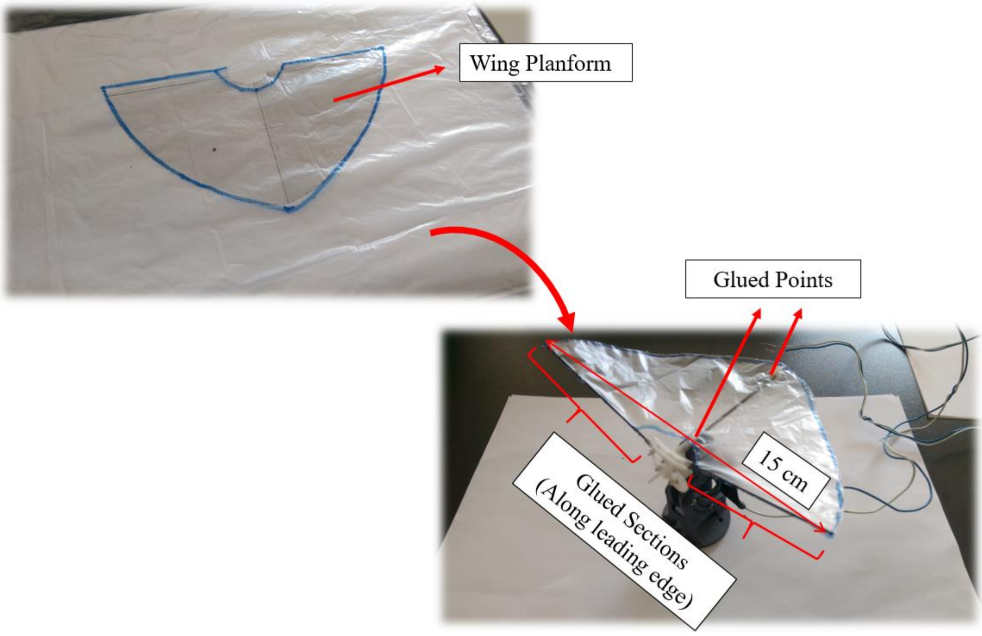

Figure 3.29: Wing membrane implementation on the utilized Flapping wing mechanism

The developed test stand is oriented to be suitable for use in the characterization of the lift force test. The prepared test setup is shown in Figure 3.30. The flapping mechanism is driven by a DC motor, and no speed or voltage control technique is applied to the utilized electric motor. In the aforementioned sections (3.3), it is implied that the wings reach 22.8 Hz of beating frequency when the flapping mechanism is driven by the electric motor at 3V. However, after wing-membrane attached to the flapping wing mechanism, the inertial loads that DC motor has to overcome increase, and subsequently, the flapping speed at 3V is reduced from 22.8 Hz to 21.2 Hz.

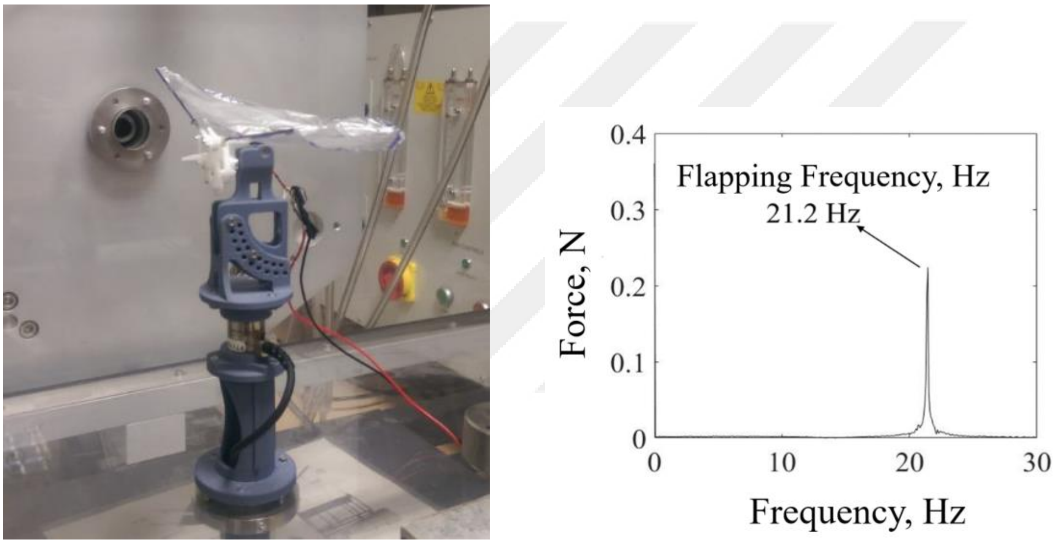

a b

Figure 3.30: Flapping test a) Lift force measurement b) Flapping frequency

3.4.2 Fluid-Structure Interaction (FSI) Analysis

A FSI analysis study involving dynamic structural finite element analysis and computational fluid dynamics is conducted to validate the flapping wing test (including the wing membrane). FSI analysis method is a ubiquitous way of understanding how fluid surrounds a body that affects the dynamic behavior of an elastic body. It combines the structural dynamics and Navier-Stokes equation and gives detailed results about the interaction between an elastic body and fluid medium. In this framework, both structural dynamics and computational fluid dynamics domains are created and communicated with each other with a $5x10^{-4}$ second of time increment for the corresponding flapping-wing model. A brief discussion about the structural dynamics finite element model is given in the previous section (3.3.3). In addition to the dynamic model aforementioned in section (3.3.3), a high-density polyethylene (HDPE) material nylon freezer bag with a thickness of 10 microns is implemented on the flapping wing mechanism. The material properties found at [55] are defined for the wing-skin material in the structural dynamics model (0.56 GPa).

Moreover, to understand how the elasticity of the wing membrane affects the aerodynamic characteristic of the proposed wing, a distinct dynamic FSI model is created utilizing high rigidity material properties (Young Modulus: $1x10^{6}$ MPa) for the wing membrane. The results obtained from high rigidity and elastic model are compared, and how the rigidity of the wing membrane influences the aerodynamic forces generated in lift and thrust force directions are reported. The structural dynamics and fluid dynamics models are given in Figure 3.31 and Figure 3.32, respectively. For the structural dynamics model ABAQUS CAE 6.14, for the CFD domain STAR CCM+ is used.

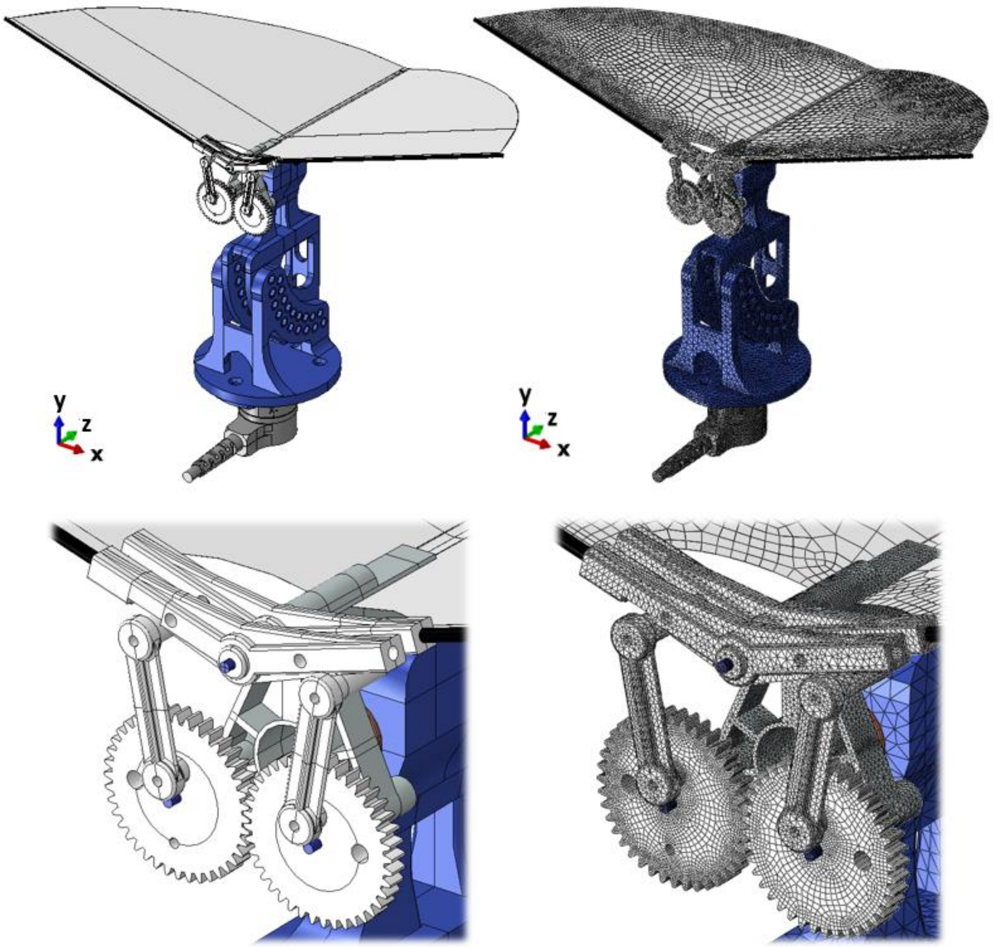

Figure 3.31: Structural dynamics model

For the computational fluid dynamics (CFD) model, wing membrane and carbon-fiber leading edge are defined, and aerodynamic contribution of the corresponding parts is investigated. The created CFD domain includes the mesh refinement regions are given in Figure 3.32.

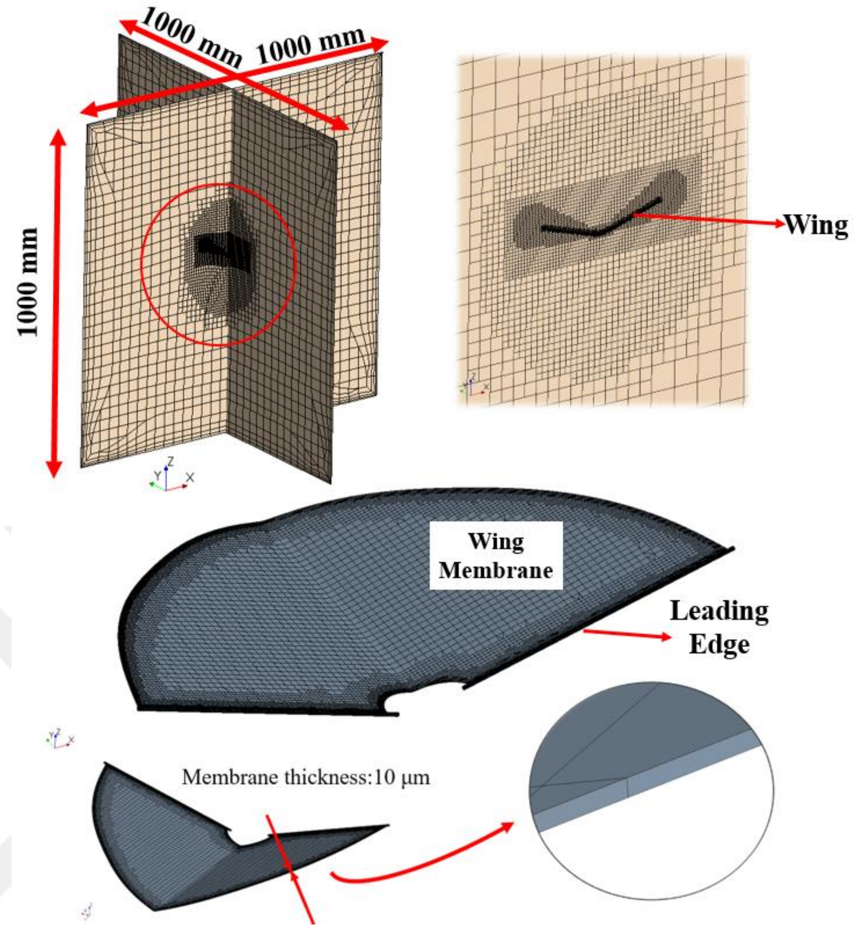
1000 mm
1000 mm
1000 mm
Wing
Wing
Membrane
Leading
Edge
Membrane thickness:10 μm

a

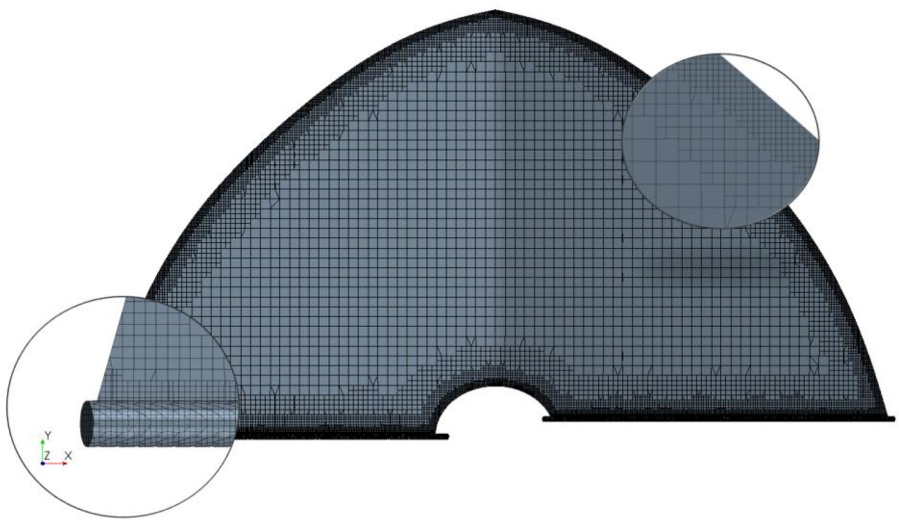

b

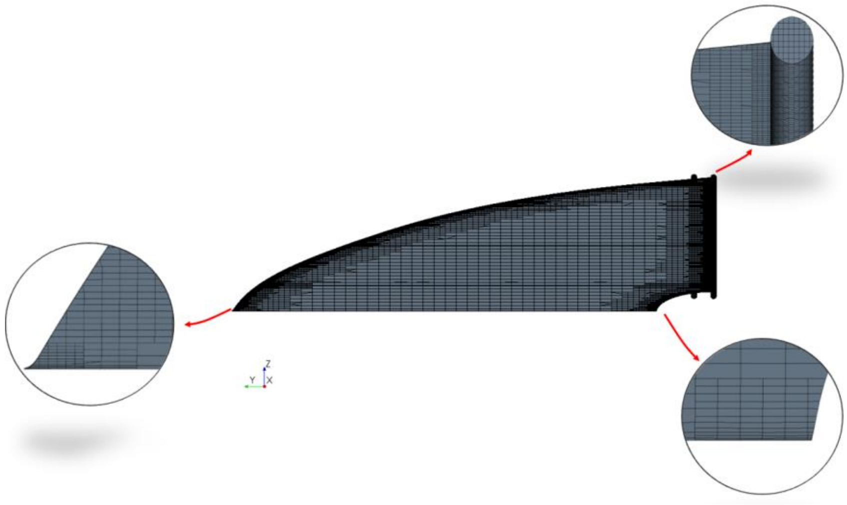

c

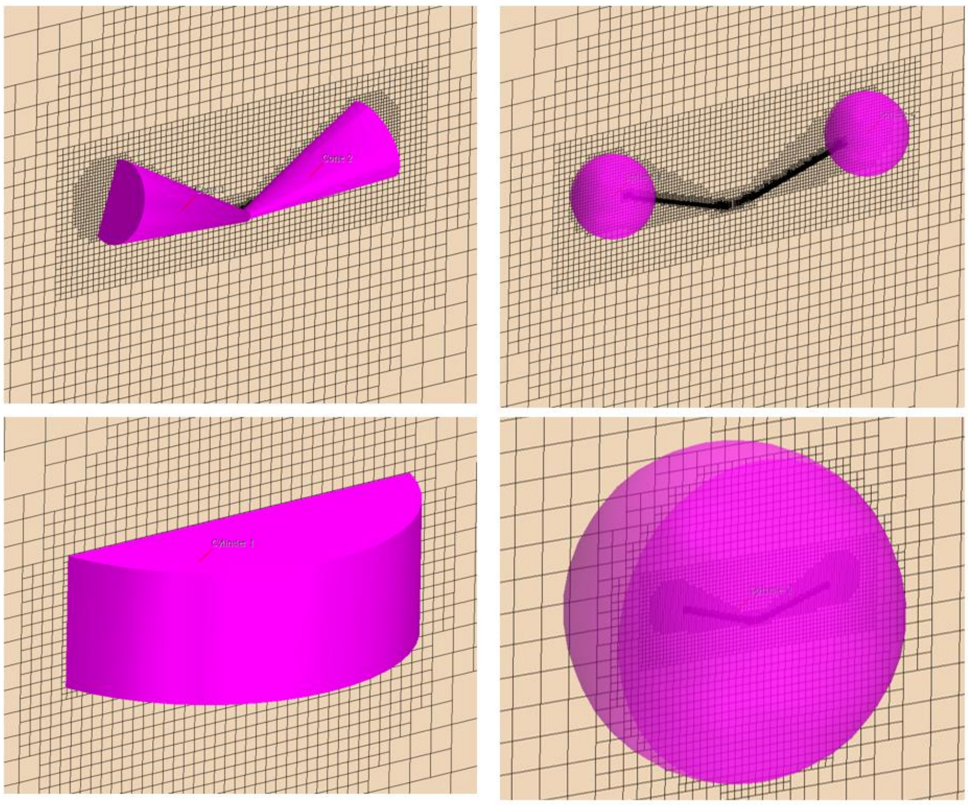

d

Figure 3.32: CFD Model a) CFD Domain b) Mesh refinements assigned to the wing (Top View) c) Mesh refinements assigned to the wing (Side View) d) Mesh refinements applied to the CFD domain

Reynolds number is calculated for the proposed flapping model to assign a computational model to the CFD domain. Reynolds number defines the ratio between inertial forces and viscous forces for a specific fluidic application. The most known form of the Reynolds number is defined as (19) for a given reference length (L_{ref}) and velocity (U_{ref}) where ν is the kinematic viscosity of the fluid at a specific temperature.

$$Re = \frac{\text{Uref Lref}}{\nu} \tag{19}$$

Shyy et al. [56] presents the Reynolds number for the 3D flapping wing application named as R_{f3} as it is given in (20)

$$Re_{f3} = \frac{\text{Uref Lref}}{\nu} = \frac{2\phi f R c_m}{\nu} = \frac{2\phi f R^2}{\nu}\left(\frac{4}{AR}\right) \tag{20}$$

Where cm, R, ϕ, f, and AR represents mean chord length, wing length, wing beat amplitude (rad), and aspect ratio (AR) of the wing. The AR and mean aerodynamic chord of the utilized elliptical planform is found out based on [57] (Pradyumna, S. V., 2015) For the given wing characteristics in Figure 3.33, the Reynolds number is found out as 1832 which lies on the laminar regime.

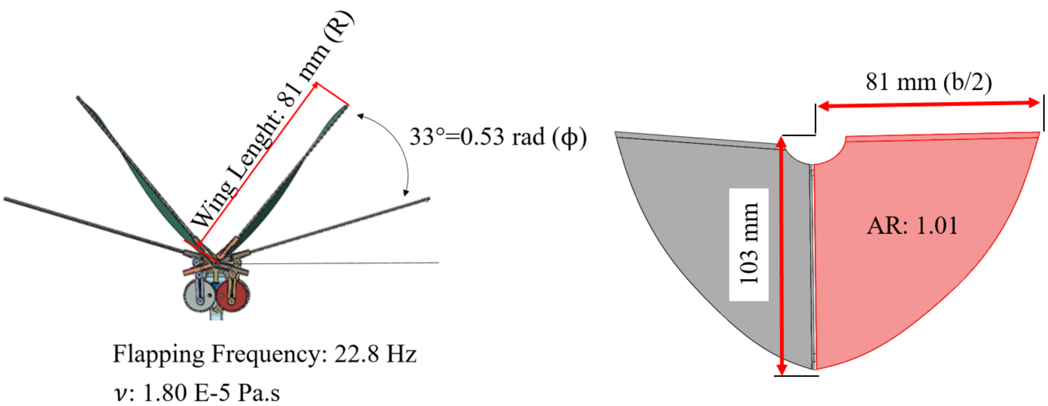

Figure 3.33: Characteristic properties of the utilized elliptical planform wing

In this regard, a laminar, three-dimensional, incompressible Navier-Stokes (21) properties defined in the CFD model.

$$\frac{du}{dx} + \frac{dv}{dy} + \frac{dw}{dz} = 0 \tag{21.a}$$

$$\rho\left(\frac{du}{dt}+u\frac{dv}{dx}+v\frac{du}{dy}+w\frac{du}{dz}\right)=-\frac{dp}{dx}+\mu(\frac{d^2u}{dx^2}+\frac{d^2u}{dy^2}+\frac{d^2u}{dz^2}) \quad (21.b)$$

$$\rho\left(\frac{dv}{dt}+u\frac{dv}{dx}+v\frac{dv}{dy}+w\frac{dv}{dz}\right)=-\frac{dp}{dy}+\mu(\frac{d^2v}{dx^2}+\frac{d^2v}{dy^2}+\frac{d^2v}{dz^2}) \quad (21.c)$$

$$\rho\left(\frac{dw}{dt}+u\frac{dw}{dx}+v\frac{dw}{dy}+w\frac{dw}{dz}\right)=-\frac{dp}{dz}+\mu(\frac{d^2w}{dx^2}+\frac{d^2w}{dy^2}+\frac{d^2w}{dz^2}) \quad (21.d)$$

CHAPTER 4

INERTIAL AND AERODYNAMIC CHARACTERIZATION RESULTS

4.1 Inertial Characterization Results

4.1.1 Experimental Results

A flapping wing experiment is conducted to measure the standalone inertial force produced by the flapping wing mechanism at zero angle of attack as it is given in Figure 4.1. In this regard, the major aerodynamic force generation source is neglected and the wing membrane is excluded.

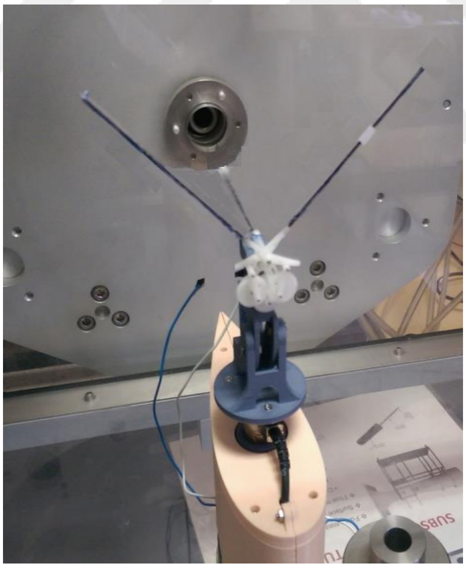

Figure 4.1: Experimental test for the flapping wing mechanism without wing membrane

FFT result shows that the structural vibration of the test platform parts have a dominant contribution to the measured force. Peripheral effects, loosen bolts, gear tooth-mesh frequencies, and shaking instrumentation cables can be given an example for the reason for the redundant forces appear at high frequency. Nevertheless, the excitement of the test stand to its natural frequency can be given as a strong body of evidence for non-moving elements has a major contribution to the measured data due to structural vibration caused by the body of the test stand. Compared to the modal analysis result, the FFT results confirms that the test stand shows unstable dynamic characteristic around 70 Hz.

As a consequence, the proposed test stand is excited to its natural frequency and creates residual forces regardless of generated inertial loads by the flapping mechanism, as given in Figure 4.2. In further sections, the theoretical calculations and the FEA result only cover the moving parts at 22.8 Hz and do not cover the forces that occur due to structural vibration of the test stand. In this manner, the redundant forces caused by vibration of the test stand is filtered using 33 Hz cut-off frequency for an accurate test-theory and analysis comparison. Then the amplification error ratio found for the utilized sensor at 3V (1/1.93) is applied to the filtered test data.

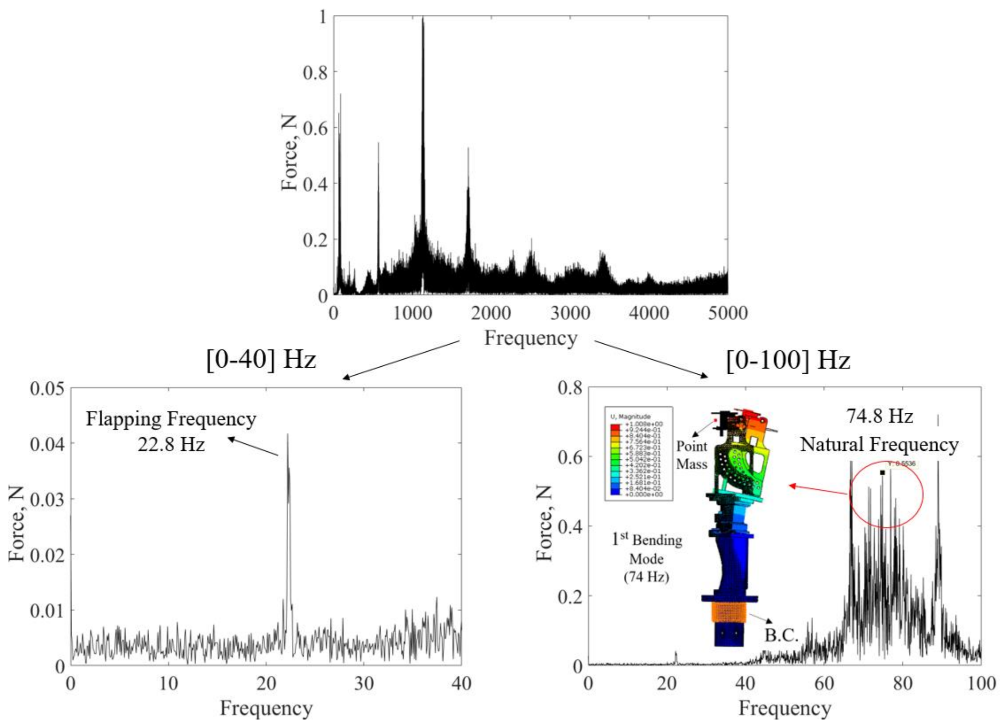

Figure 4.2: FFT of the conducted flapping test

The filtered-corrected (multiplied by 1/1.93) and the filtered-uncorrected test force results obtained for the y-axis (Figure 3.28) are given in Figure 4.3.

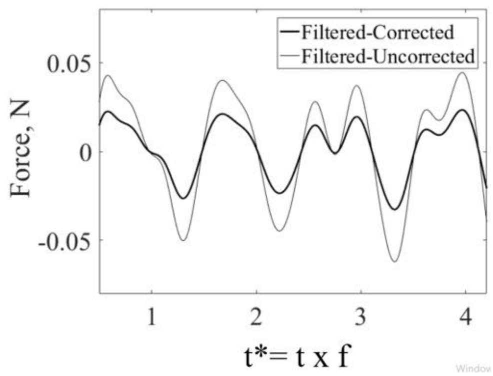

Figure 4.3: Uncorrected and corrected form of the filtered test result

4.1.2 Inertial Force Calculation Results

Theoretical calculations associated with finding the total produced inertial force in the lift direction (y-axis, Figure 3.28) are employed for each part given in Table 3-4 by utilizing the governing equations given in (15) and (17). The obtained inertial force results for the corresponding parts are given in Table 4-1, Table 4-2, and Table 4-3, respectively.

.

Table 4-1: Inertial force investigation for Part-I

<table>
<tr><th colspan="2">Part-I</th></tr>
<tr><td colspan="2">The part1 rotates about the O_1 axis at a constant speed. Since it has constant rotation speed (w) around a specific radius (r_1), the rate of change of radius and angular velocity is zero, and only the centrifugal force is calculated.
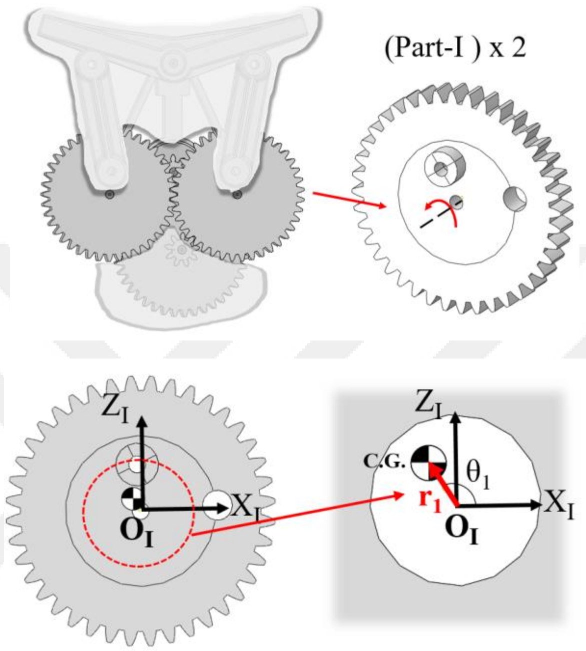
</td></tr>
<tr><td>Angular travel of the mass center of part I</td><td>The inertial force created by part I in vertical (y) direction</td></tr>
<tr><td>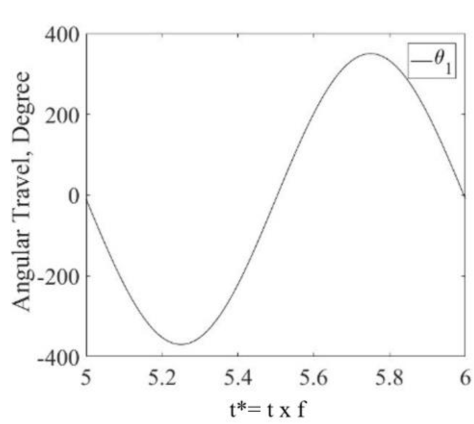
</td><td>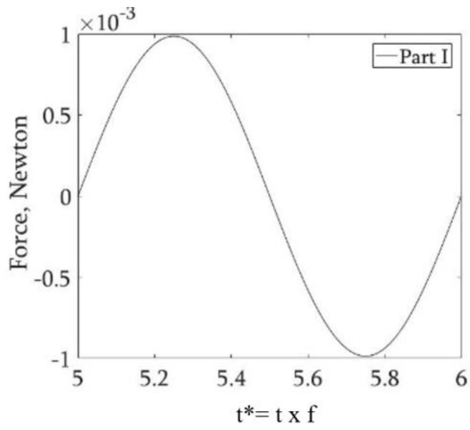
</td></tr>
</table>

Table 4-2: Inertial force investigation for Part-II

<table>
<tr><th colspan="2">Part-II</th></tr>
<tr><td colspan="2">Part II follows an elliptical trajectory, as illustrated below. The instantaneous radius, velocity, and acceleration terms change along with its motion. In this regard, pure curvilinear motion is investigated, and inertial terms are calculated for part II concordantly. The time-dependent velocity and acceleration values are found via implementing dynamic FEA analysis results, and plugged into the coriolis terms belongs to governing rigid-body dynamic equation.</td></tr>
<tr><td colspan="2">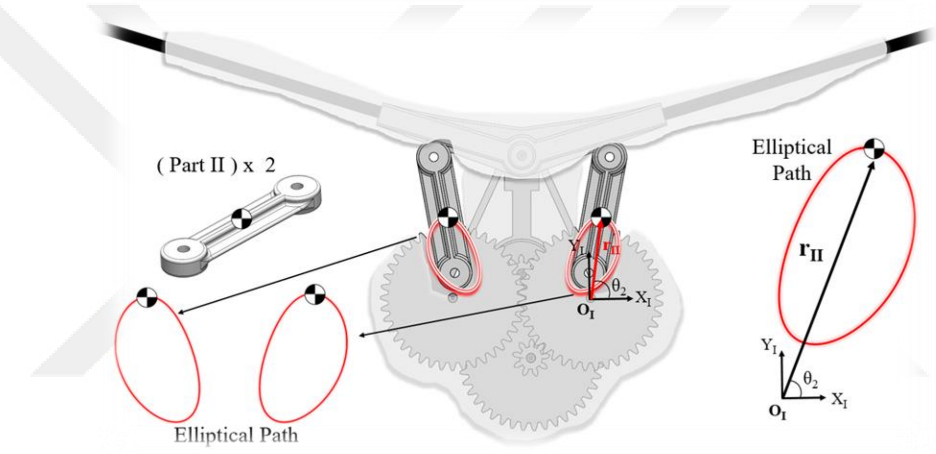
</td></tr>
<tr><td>Angular travel of the mass center of Part II</td><td>The inertial force created by Part II in vertical (y) direction</td></tr>
<tr><td>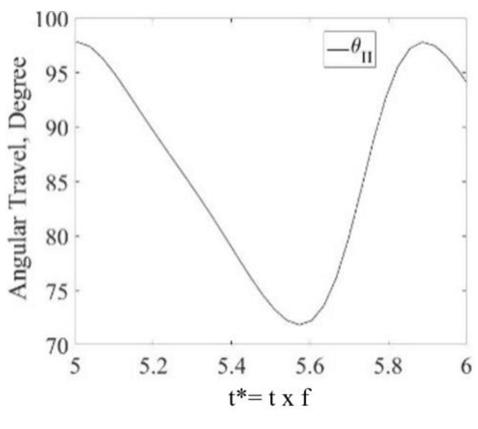
</td><td>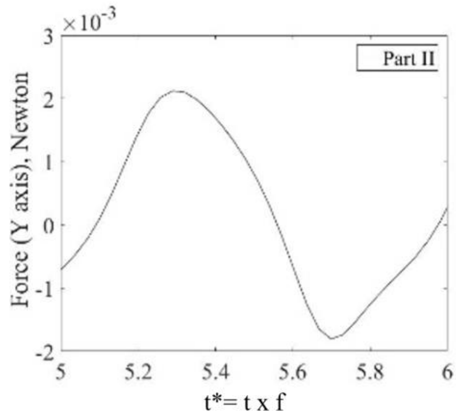
</td></tr>
</table>

Table 4-3: Inertial force investigation for Part-III & IV

<table>
<tr><th colspan="2">Part-III & IV</th></tr>
<tr><td colspan="2">Part III & IV attached and assumed as a combined part rotates around O_{III} with a radius of $R_{III\text{-}IV}$(0.011 m). Unlike part-I, during flapping motion, part III & IV accelerates and decelerates at the end of each upstroke and downstroke phase of the flapping motion. Thus, in addition to the centrifugal force, the corresponding part experiences an angular acceleration, and subsequently, a tangential force term arises during the flapping motion.
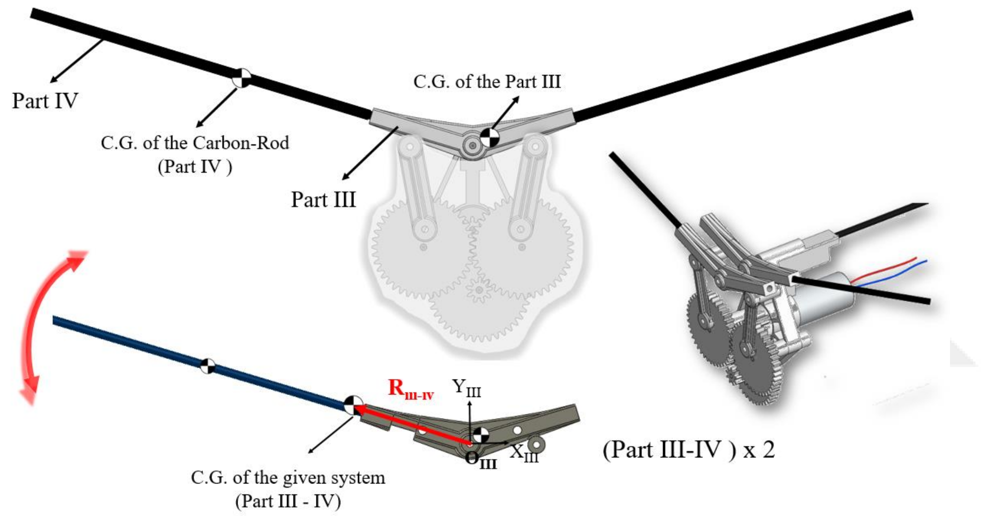
</td></tr>
<tr><td>Angular travel of the mass center of Part III & IV</td><td>The inertial force created by Part III & IV in vertical (y) direction</td></tr>
<tr><td>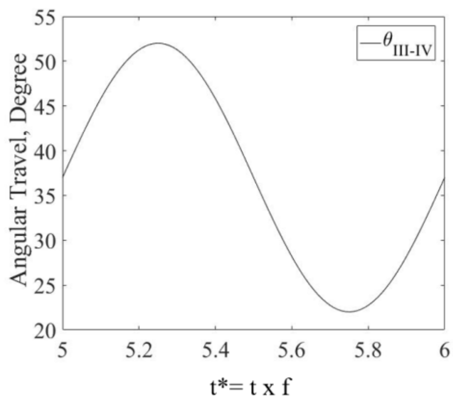
</td><td>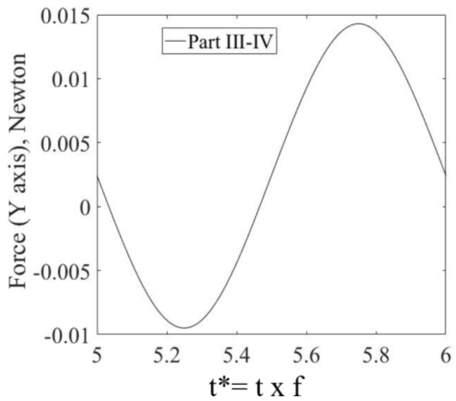
</td></tr>
</table>

4.1.3 Dynamic Finite Element Analysis

A dynamic finite element analysis is performed for the corresponding flapping mechanism model. Visualizations regarding dynamic analysis results for t*=1, t*=1.24, and t*=1.48 are given in Figure 4.4.

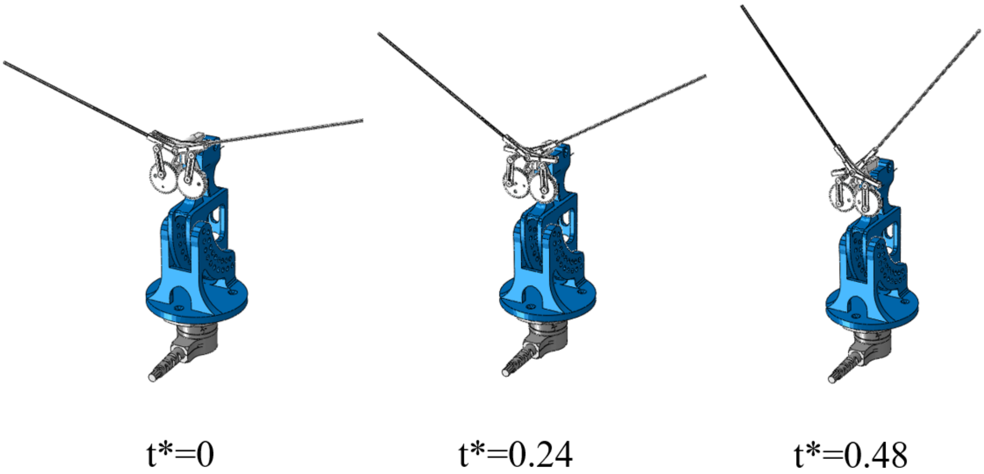

Figure 4.4: Time-dependent visualizations of the performed dynamic finite element analysis result

The comparison of inertial force generated by the flapping wing mechanism acquired from experimental, theoretical, and FEA approach is given in Figure 4.5a for t* between 1 and 4. A good agreement between experimental, theoretical, and numerical study is achieved. The dynamic FEA and theoretical force results were decomposed into frequency domain, as given in Figure 4.5 bc, respectively. Due to the nonlinear force response of the FEA, a visible difference is observed between the FEA and theoretical approaches (Figure 4.5a). When the higher-order harmonics that occured in FEA (Figure 4.5b) and theoretical approach (Figure 4.5c) are filtered, a close match between two methods is obtained (Figure 4.5d).

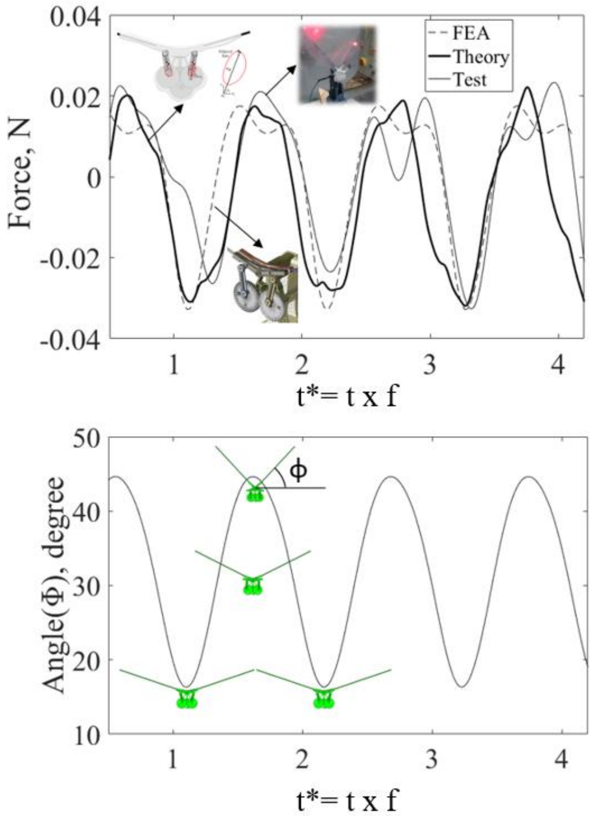

a

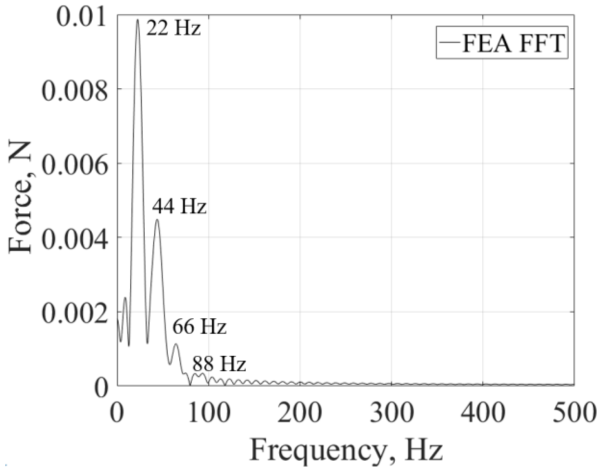

b

Figure 4.5: Inertial characterization results a) Comparison of the experimental, FEA and theoretical force results in the y-direction (Figure 3.20) b) FFT result (FEA) c) FFT result (Theory) d) Comparison of the theoretical and FEA results excluding the effect of harmonic frequencies

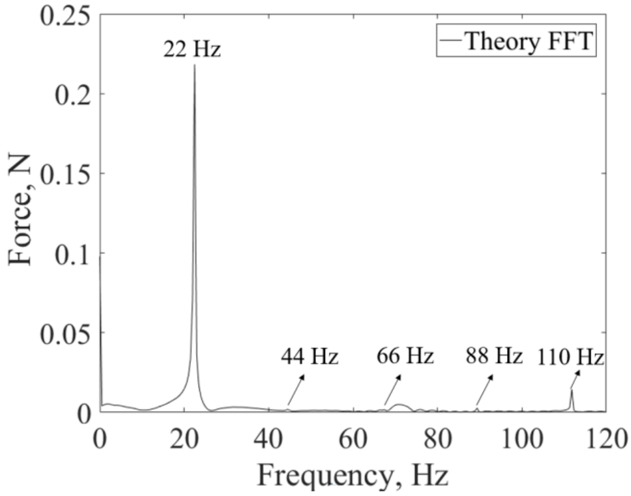

c

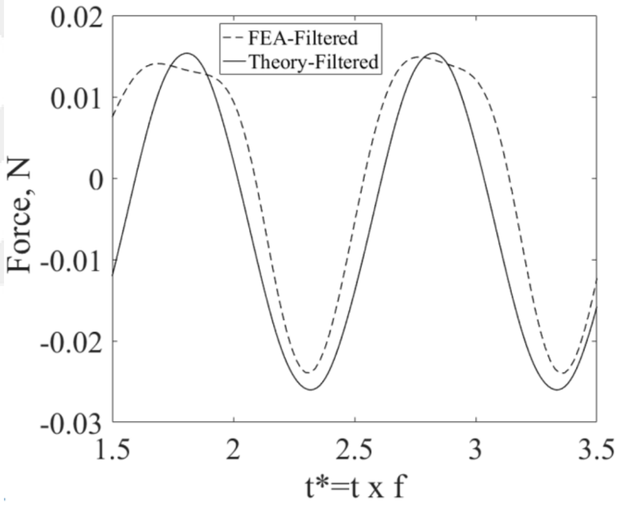

d

Figure 4.5 cont’d

4.2 Aerodynamic Characterization Results

4.2.1 Experimental Results

In the aerodynamic characterization section, a nylon cover wing membrane is attached to the corresponding flapping mechanism. Experiments associated with the understanding of the aerodynamic lift force generation capability of the utilized flapping wing mechanism is investigated. The upmost and lower position achieved by the leading-edge of the utilized flapping mechanism is given in Figure 4.6.

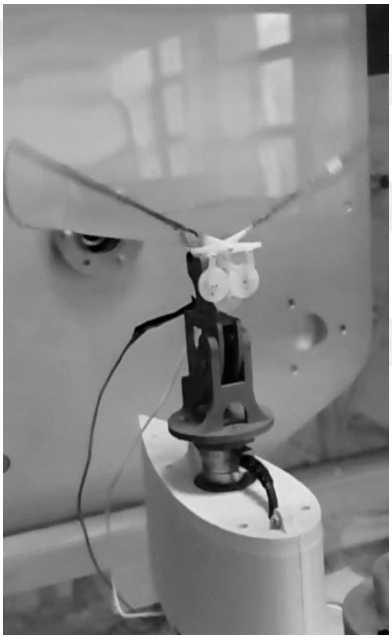

a

b

Figure 4.6: Different stroke positions of leading-edge occurred during the flapping test a) Lower position of the leading edge b) Utmost position of the leading edge

Butterworth filter method with 33 Hz cut-off frequency and the amplification factor (1/1.93) is applied to the raw test data. The filtered-uncorrected and the filtered-corrected (multiplied by 1/1.93) lift force data are given in Figure 4.7.

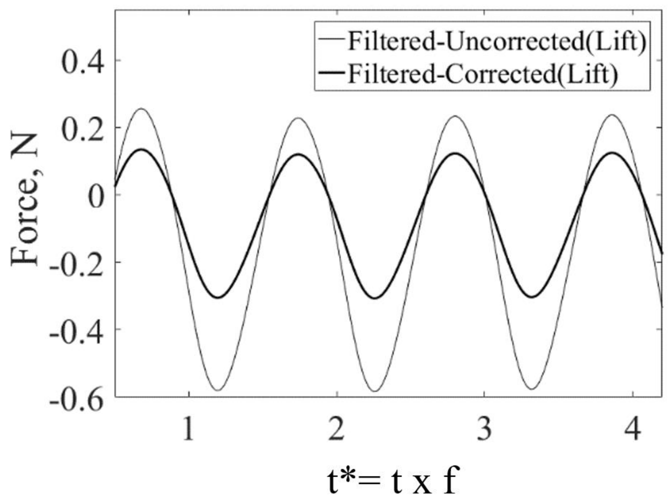

Figure 4.7: Filtered, corrected and uncorrected test results a) Lift force result b) Thrust force result

4.2.2 Fluid-Structure Interaction (FSI) Analysis Results

A FSI study regarding verify the conducted flapping experiment results given in section 4.2.1 is performed. The visualizations of the performed FSI study for t*=1, t*=1.24, and t*=1.48 given in Table 4-4 for the structural dynamics and the CFD domain. According to the results obtained from FSI analysis (Figure 4.8), a close resemblance is achieved to the conducted flapping experiment results in the previous section. In Figure 4.8, the total lift force represents the time-dependent summation of the aerodynamic and inertial results that is exerted on the force sensor, the aerodynamic lift force in Figure 4.8, represents the total force generated by both wings in CFD domain and does not include the inertial force created by mechanism parts. Since the model is oriented for zero angles of attack without undergoing any air stream, a negative lift force result is obtained.

Table 4-4: Visualization of the FSI analysis results for both domains

Domain	t*=1	t*=1.24	t*=1.48
Structural Dynamics Domain	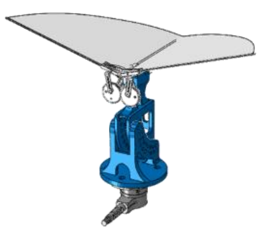		
CFD Domain	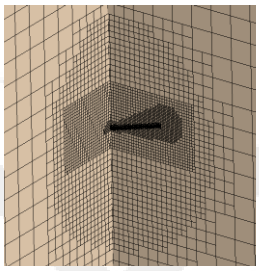	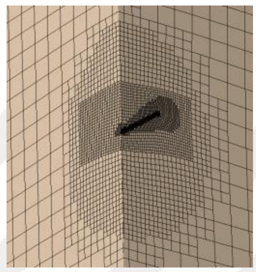	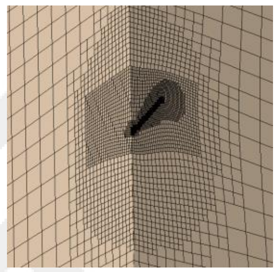
			

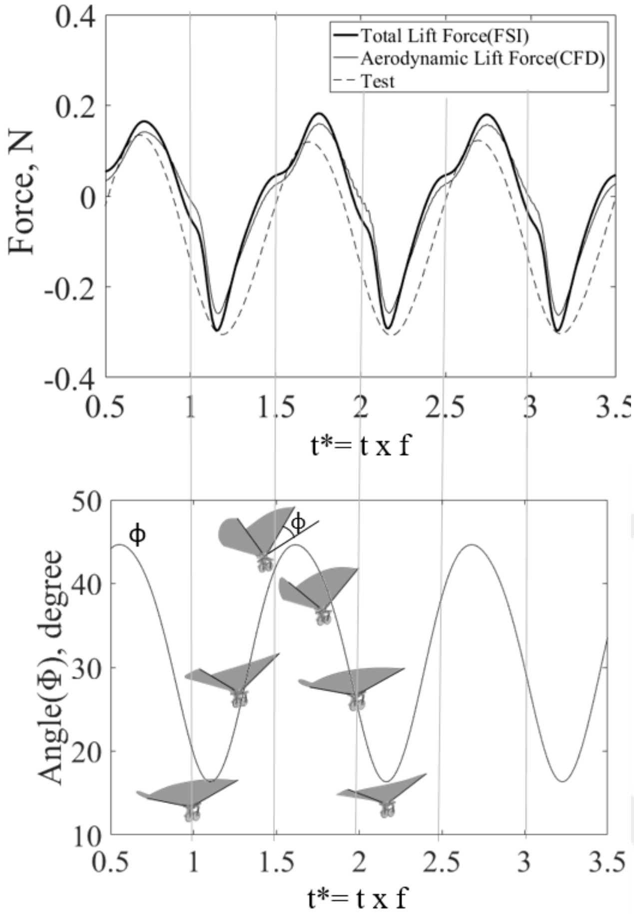

Figure 4.8: FSI-Test comparison for the lift force results

4.2.3 Wing-Flexion Effect on Aerodynamic Performance

A distinct FSI analysis model with high rigidity material properties is created to understand how the wing-flexion affects aerodynamic performance during flapping motion. The corresponding results are compared to the elastic wing model for the lift and thrust forces results. Table 4-5 visualizes the occurred wing deformation for both rigid and elastic models between t*=2 and t*= 3. A notable wing deformation difference appears between elastic and rigid wing models during the flapping motion.

Table 4-5: Time-dependent wing deformation occurs on high-rigidity and elastic models

t*	High Rigidity Model	Elastic Model
2.0		
2.18		
2.36		
2.54		
2.72		
2.91		
3		

Tip displacement (Δz), instantaneous flapping angle (φ), lift force, and thrust force are compared for the FSI analysis cases performed for the rigid and elastic model and given in Table 4-6. The elastic wing model creates a more negative force (t*=2-2.2) comparing to a rigid model at the end of the downstroke motion (zero angles of attack, no stream velocity). However, it restores the negative lift force earlier than the rigid model and reaches a greater level of positive lift force. The elastic model shows greater performance for generating a thrust force and shows full thrust characteristics throughout the full cycle. On the contrary, a rigid model mostly performs negative thrust (y) to the reference axis (Table 4-6).

Table 4-6: Tip displacement, angular travel, and force comparison of the rigid and elastic model

<table>
<tr><td colspan="2">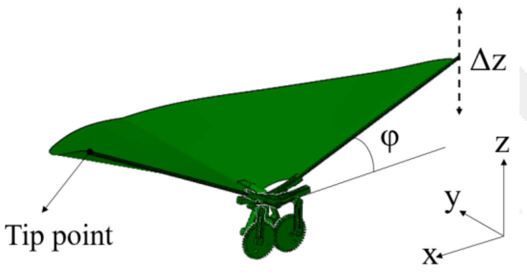
</td></tr>
<tr><td>Tip displacement and angular travel</td><td>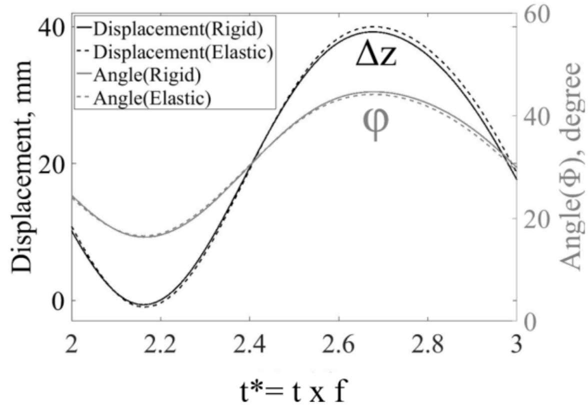
</td></tr>
</table>

Table 4-6 (cont'd)

Lift	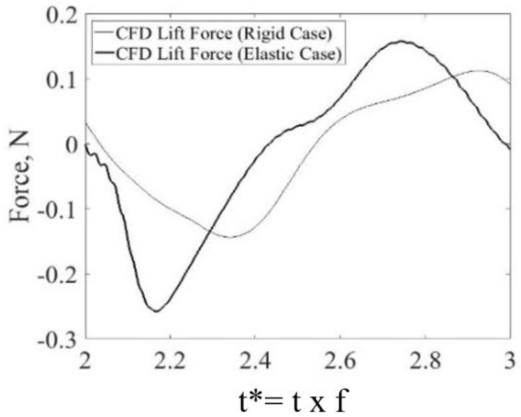
Thrust	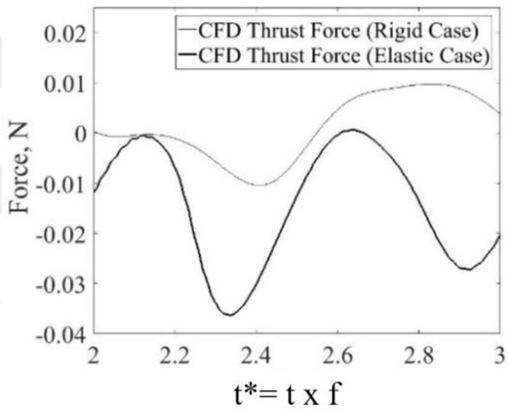

The wing deformation occurs on the elastic and high-rigidity model are investigated for a chosen cross-section given in Table 4-7. Both models show a distinct characteristic in terms of time dependent chord-wise displacement.

Table 4-7: Comparison of cross-sectional wing behavior of rigid and elastic models

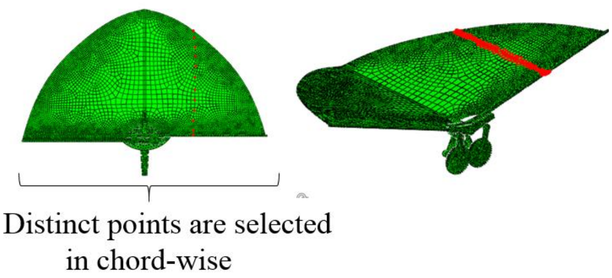

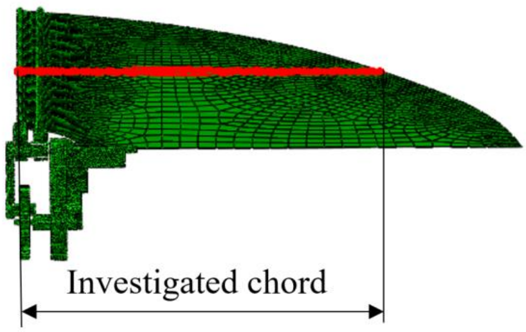

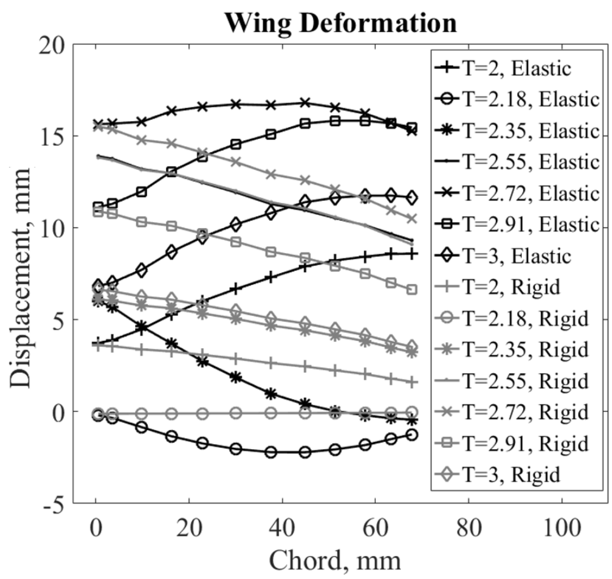

4.3 Flow Structures

Vortical structures and lift generation are interpreted at selected instants during the performed flapping motion as a down-stroke and up-stroke phase, as it is given in Figure 4.9.

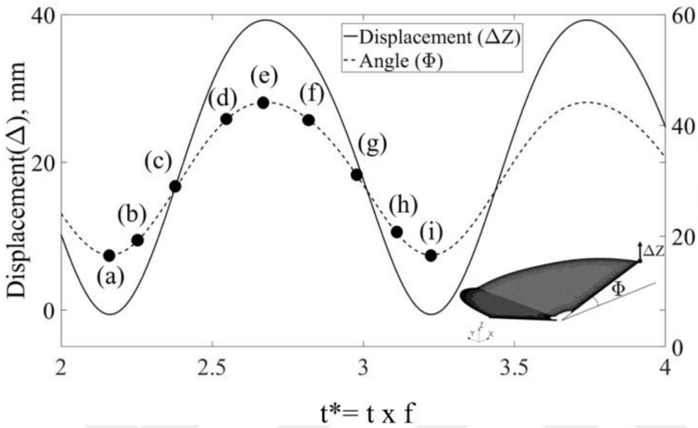

I

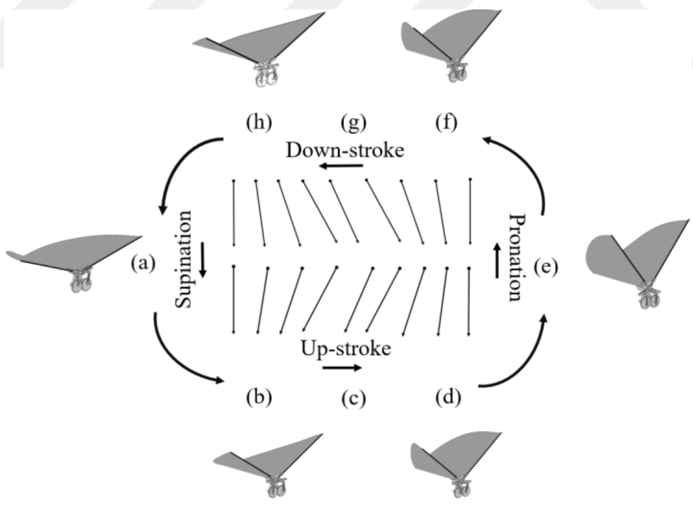

II

Figure 4.9: Time history of the performed flapping motion (flapping angle (φ), tip displacement of the leading edge (Δz)). I) a) Late pronation (t*=2.16) b) early downstroke (t*=2.27) c) middle downstroke (t*=2.4) d) late Downstroke (t*=2.55) e) early supination (t*=2.68) f) late supination (t*=2.80) g) early upstroke (t*=2.98) h) late upstroke (t*=3.11) i) Early pronation (t*=3.22) II) Visualization of the computed flapping motion

The vorticity and pressure contour plot results are given for t* between 2 and 3 in Table 4-8 and Table 4-9, respectively.

Table 4-8: Vorticity contour plots for t* between 2 and 3

t*	High Rigidity Model	Elastic Model
2.0	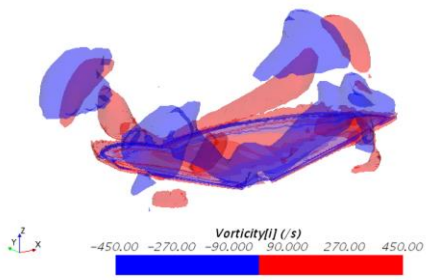	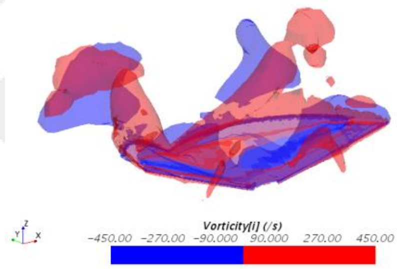
2.16 (a)	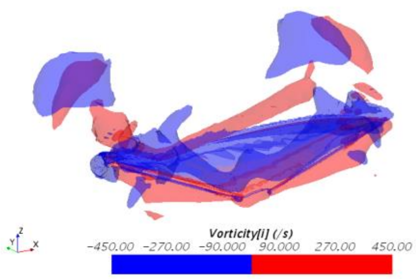	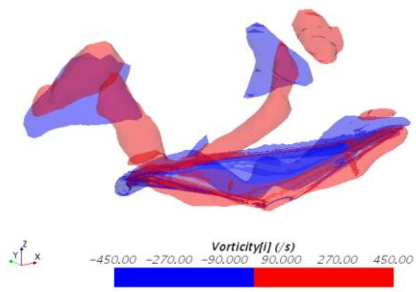
2.27 (b)	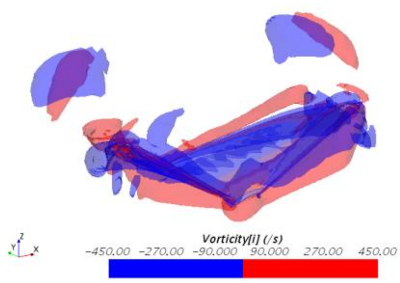	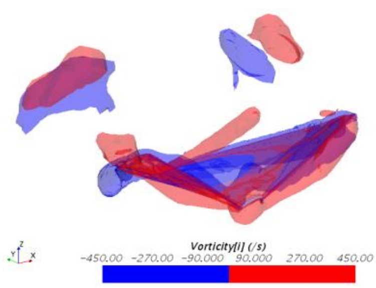

Table 4-8 (cont'd)

<table>
<tr><td>2.4
(c)</td><td>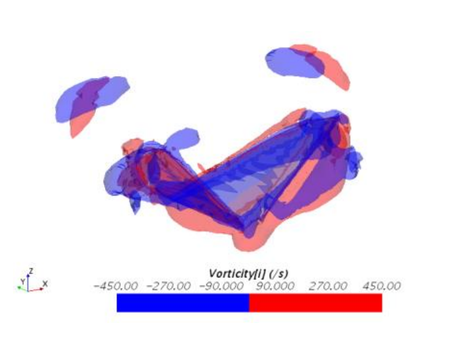
</td><td>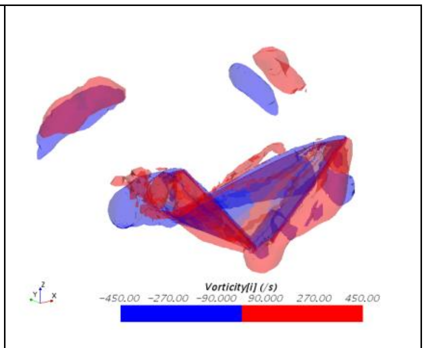
</td></tr>
<tr><td>2.54
(d)</td><td>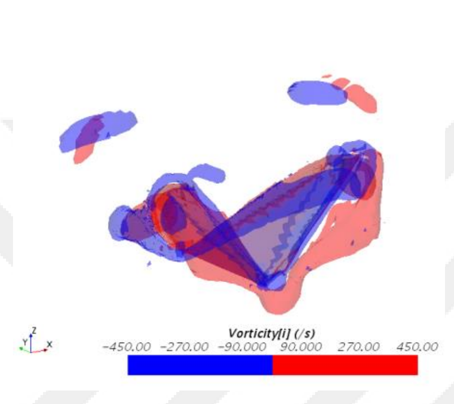
</td><td>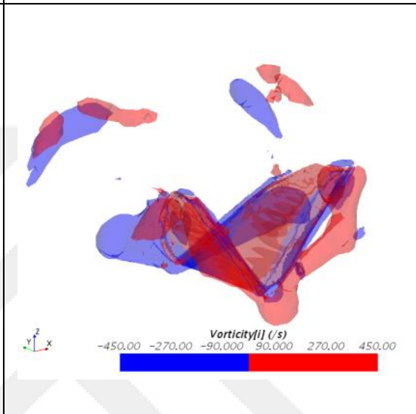
</td></tr>
<tr><td>2.68
(e)</td><td>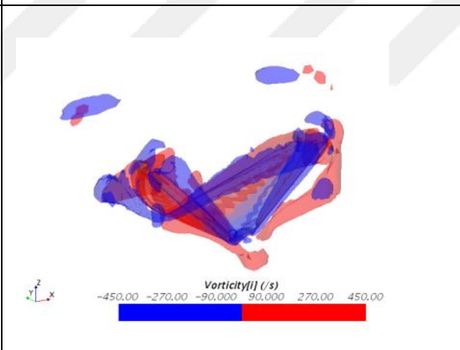
</td><td>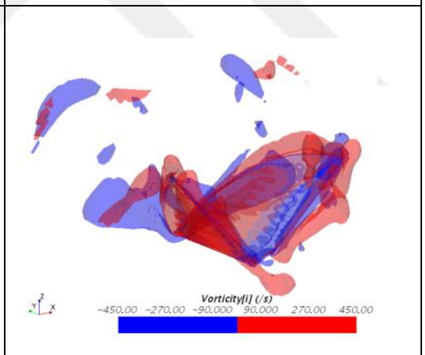
</td></tr>
<tr><td>2.80
(f)</td><td>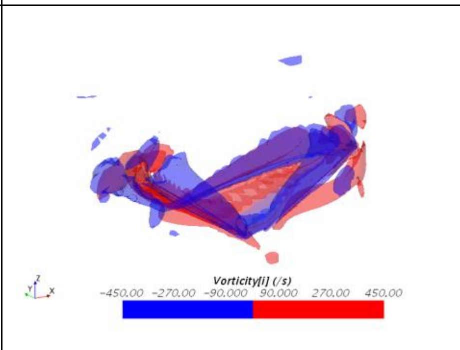
</td><td>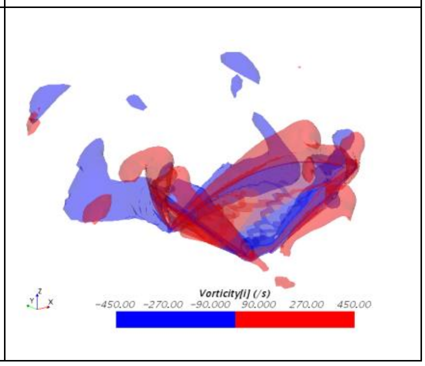
</td></tr>
</table>

Table 4-8 (cont'd)

2.98 (g)	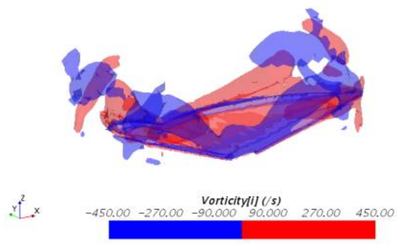	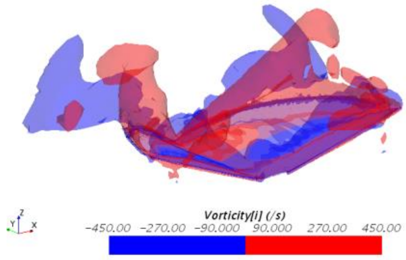
3.11 (h)	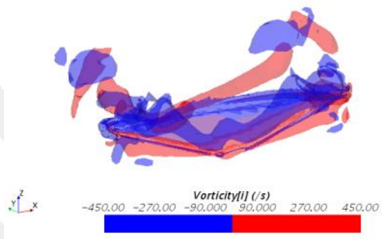	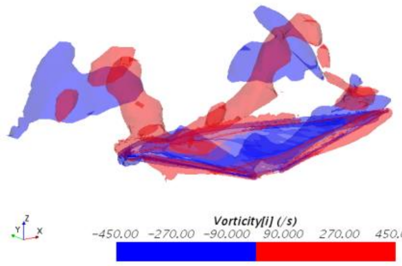

Table 4-9: Pressure contour plots for t* between 2 and 3

t*	High Rigidity Model	Elastic Model
2.0	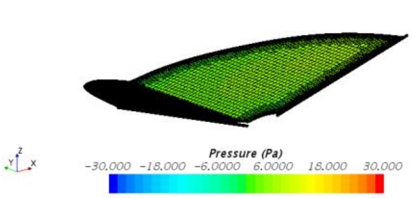	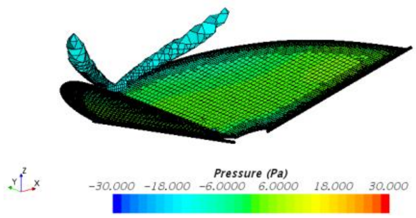
2.16 (a)	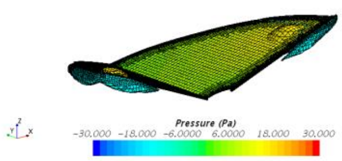	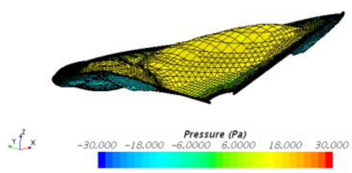

Table 4-9 (cont'd)

2.27 (b)	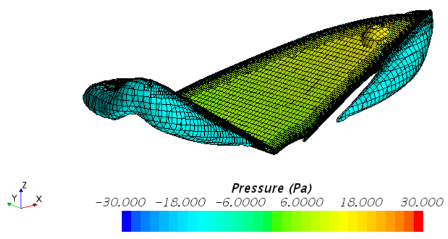	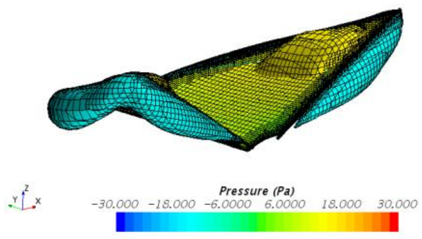
2.4 (c)	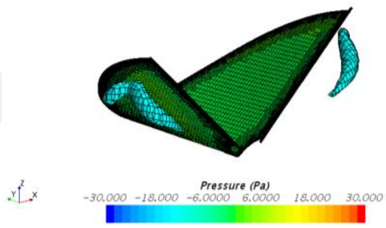	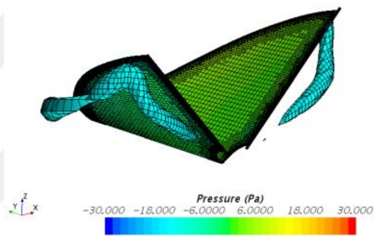
2.54 (d)	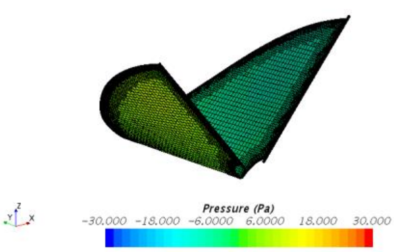	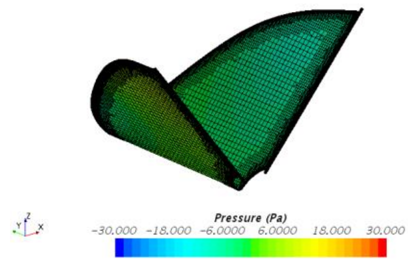
2.68 (e)	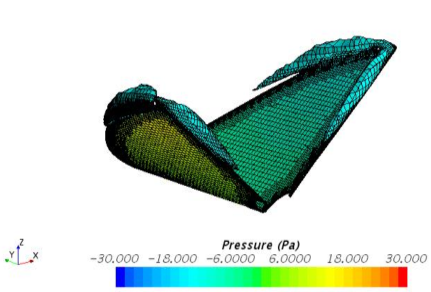	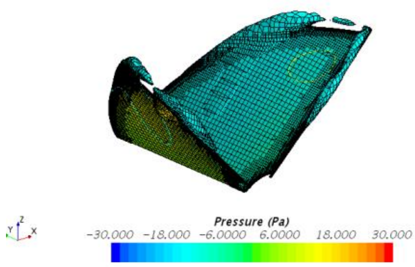

Table 4-9 (cont’d)

2.80 (f)	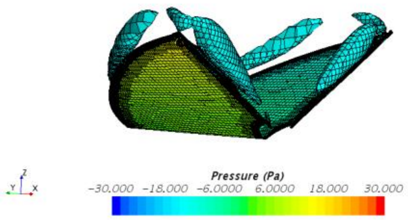	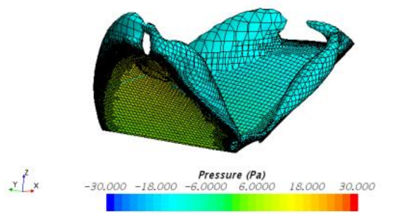
2.98 (g)	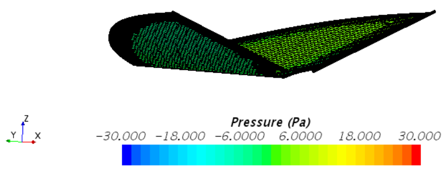	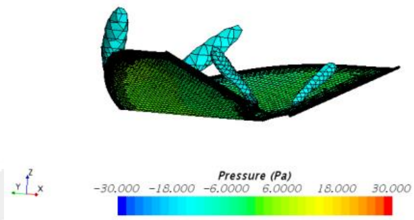
3.11 (h)	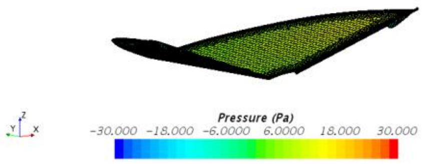	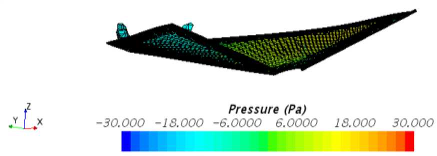

4.3.1 Flow Structures During Upstroke:

Upstroke phase initiates right after the supination and it and covers the intervals between (a) and (e) depicted in Figure 4.9 I. At the beginning of the upstroke implied as point (a), dominant residual vortex form is observed around the wing edges due to previous impulsive flapping sequence. In the initial of the upstroke phase (a), a minute level of vortex structures accumulates towards under the leading edge in both rigid and elastic model. Higher pressure region is observed on the elastic wing compared to the rigid wing. Even though, both model shows similar vortex characteristic at the beginning of the upstroke in terms of shape form and size of the trailing and leading-edge vortex structures, as the wing sweeps reach from (b) to (e), leading-edge vortex (LEV) and trailing edge vortex (TEV) enlarges. During the flapping-wing reaches from (b) to (e), a rapid pressure reduction is observed on the elastic wing surface, on the other hand, the rigid model does not show significant pressure alteration on the wing surface. For both models, a developing lower pressure region surrounds the leading-edge with an offset is monitored as the wing sweeps through (b)-(c)-(d) points. However, it disappears as the wing ends up its upstroke motion (e). All through the upstroke motion (b to e), positive (red-colored) vorticity components (+x) dominates around the leading-edge of the elastic wing. On the other hand, the combination of positive (red-colored) and negative (blue-colored) vorticity components develop simultaneously around the leading-edge of the rigid wing, as it is illustrated in Figure 4.10 for the point (c). It is concluded that the wing-flexion leads to the discharge of the negative vortical structures around the trailing edge and creates bigger trailing edge structures around the wing edges. On the contrary, the rigid wing model suffers from discharging the high-pressure region from its trailing edge, and either it stores on its wing surface or trying to discharge from its leading-edge section. As a consequence, rapid pressure change occurs on the elastic wing, and subsequently, higher lift force augmentation is attained on the elastic wing model compared to the rigid wing model between (b) and (e) intervals.

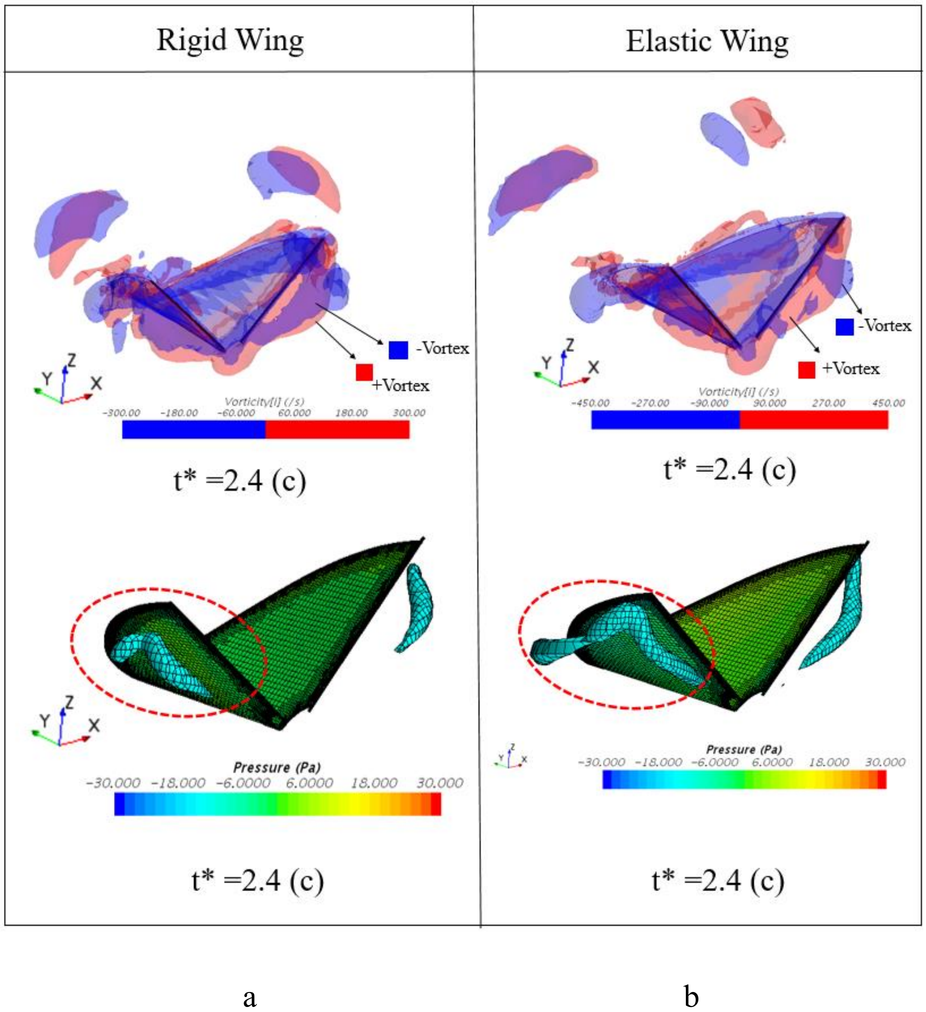

Figure 4.10: Direction of vortical structures and pressure distributions occur on the flapping wing for mid-upstroke (c) a) Rigid wing model b) Elastic wing model

Throughout the down-stroke motion, thrust force results show uneven characteristics for both models (rigid & elastic). The orientation of the FSI model is aligned as the negative y-axis defines full thrust concerning the flying direction (Table 4-6). In the first half of the up-stroke ((a)-(c)), both models develop short-term thrust force with a different growth rate. However, the elastic wing model contributes more to the achieved thrust force level compared to the rigid wing between (a) and (c) interval. Shortly after, the resultant thrust force starts to grow in the opposite direction and continues until the end of the upstroke motion. At the end of the upstroke motion, the elastic model preserves its positive thrust attitude though nearly zero. However, the rigid wing shows completely negative thrust characteristics to the desired flight direction.

4.3.2 Flow Structures During Downstroke

Downstroke starts after the pronation phase and encompasses instants indicated in Figure 4.9 between (e)-(h). Until the wing reaches from (e) to (f), significant pressure attenuation is observed on the elastic wing surface. This situation leads to grow the vortex structures occurred around the trailing edge and generate more lift force (Figure 4.11 I). Meanwhile, the rigid wing model shows poor performance compared to the elastic wing on discharging the high-pressure region from on its wing surface and generates lower lift force between (e) and (f) (Figure 4.11 II).

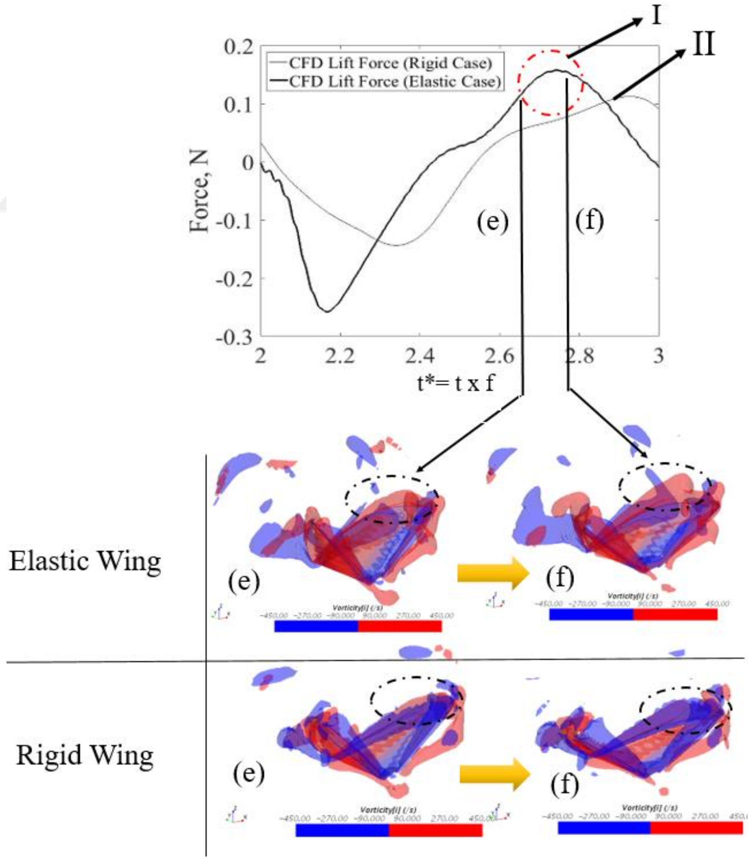

Figure 4.11: Lift force and Vortex structure generation for rigid and elastic models between (e) and (f)

The corresponding FSI analysis findings show that when the elastic wing model gets its maximum lift force value, the utmost lift force value in the rigid wing model yet unevolved. Shortly afterward, the rigid wing model passes the point (f) and reaches to the point (g), the rigid wing discharges the negative vortical structures (blue-colored), and positive vortical structures (red-colored) preserve their existence on its wing. Therefore, a slight lift augmentation is observed, and the rigid wing model reaches to its climax lift force value (Figure 4.11 II). After the point (f), the vortical structures occurred on rigid and elastic wing begins to shed from wing edges, and the generated lift force reduces between (f) and (h) (Table 4-6).

Even though the thrust force results show similar trends for both models for the down-stroke phase, it exhibits completely different force levels of magnitude. Excluding the early and late down-stroke phase, both models show a vast majority positive trend throughout the down-stroke phase. Comparing the thrust performance of elastic and rigid wing models, the elastic wing model predominantly generates greater force level and achieves full-thrust mode in the desired flying axis. However, the rigid wing model shows weak thrust performance and is not capable of creating a satisfactory level of full-thrust in the desired flying direction.

CHAPTER 5

CONCLUSION

In this thesis, the inertial and aerodynamic characterization of a generic flapping wing mechanism including verificaction studies are employed. A custom test-platform is developed for experimental purposes, and vibrational characterization of the proposed test-platform is carried out by performing modal analysis. A simplified experimental study is employed to calibrate the utilized force sensor, and the acquired error factor is applied to the raw test data. An inertial characterization study is conducted to understand the standalone contribution of the inertial forces generated by the mechanical flapper on the produced total aerodynamic lift force. Within this framework, the wing membrane is excluded, and total inertial force generated due to the motion of the prescribed kinematics in the lift direction is investigated by performing experimental, dynamic FEA and theoretical approaches. A great deal of compliance is acquired with the test, theory and, dynamic FEA results for the corresponding flapping-wing mechanism without wing membrane. Also, it is found that the difference between FEA and theoretical approach results is caused by the arisen of higher-order harmonic frequencies. For the aerodynamic characterization study, the wing membrane is implemented to the flapping wing mechanism, and a comparative study based on an experimental and a FSI analysis is performed. A high correlation between experimental and numerical study is acquired for the lift force. It is concluded that the inertial forces reduce %10 the generated aerodynamic lift force when the wing finishes its downstroke motion. Additionally, the wing flexion effect on aerodynamic performance is studied. In this framework, a distinct FSI model along flapping wing with high rigidity material properties is created and the corresponding lift results compared to the elastic model conclusions. The outcome of the performed aerodynamic force generation capability assessment between rigid-elastic wing models for hovering flight condition at zero angles of attack clearly shows that elastic wing has a tremendous influence on generation thrust force. Compared to the rigid wing model, the elastic wing generated a more positive lift force at the end of the upstroke. However, the flexible wing generated more negative lift force at the end of the downstroke. For both rigid and elastic models, thrust force generation mostly appears through the downstroke motion, and it reaches its climax with a time-lag (for t*= 2.35) difference compared to lift force (t*=2.2, where downstroke phase finishes). In this regard, the elastic wing model scatters the full-thrust characteristic throughout the flapping motion. However, the rigid wing model shows far worse performance on generating thrust force by developing a smaller level of thrust force and showing uneven characteristics throughout the flapping sequence.

During the experiments, some rigors associated with the utilized flapping wing mechanism have been experienced by the author. The occurrence of gear tooth damage due to the high friction between the contact of gear pairs and high tolerance clearance between the mechanical parts can be given an example of major pitfalls of the utilized flapping wing mechanism.

REFERENCES

[1] Michelson, R. C. 2006. Very Small Flying Machines, 2006 Yearbook of Science& Technology, McGraw-Hill, New York, pp. 341–344. ISBN: 0-07-146205-8.)

[2] Web of Science 2020. Retrieved from www.webofknowledge.com

[3] Karásek M., Muijres F. T., De Wagter, C., Remes, B. D. W., de Croon, G. C. H.E. 2018. A tailless aerial robotic flapper reveals that flies use torque coupling in rapid banked turns. Science, 361(6407):1089-1094. doi:10.1126/science.aat0350.

[4] Rosen, M. H., Le Pivain, G., Sahai, R., Jafferis, N. T., Wood, R. J. 2016 Development of a 3.2g untethered flapping-wing platform for flight energetics and control experiments. IEEE International Conference on Robotics and Automation (ICRA), Stockholm, pp. 3227-3233, doi: 10.1109/ICRA.2016.7487492.

[5] Keennon, M., Klingebiel, K., Won, H. 2012. Development of the nano hummingbird: A tailless flapping wing micro air vehicle. 50th AIAA Aerospace Sciences Meeting including the New Horizons Forum and Aerospace Exposition, p. 588, doi: 10.2514/6.2012-588.

[6] Chirarattananon, P., Chen, Y., Helbling E. F., Ma, K. Y., Cheng, R., Wood, R. J. 2017. Dynamics and flight control of a flapping-wing robotic insect in the presence of wind gusts. Interface Focus 7, 20160080, doi:10.1098/rsfs.2016.0080.

[7] Ramezani, A., Shi, X.,Chung, S. J., Hutchinson, S. 2016. Bat Bot (B2), A Biologically Inspired Flying Machine. IEEE International Conference on Robotics and Automation, Stockholm, Sweden, May 16-21, doi: 10.1109/ICRA.2016.7487491.

[8] BionicOpter, 2014, retrieved from https://www.festo.com/PDF_Flip/corp/Festo_BionicOpter/en/files/assets/basic-html/page-1.html

[9] Senol, G. 2016. Design and Testing Of a Four Analysis. Middle East Technical University Aerospace Engineering Department, MSc Thesis.

[10] Beker C, Turgut A. E., Ozcan O., Kurtulus, F. 2017. Design of a Novel Foldable Flapping Wing Micro Air Vehicle. AIAC-2017-138, 9'uncu Ankara Uluslararası Havacılık-Uzay Konferansı.

[11] Beker, C., Turgut, A. E., Arıkan, K.B., Kurtulus, D. F. 2019. Fluid-Structure Interaction of a Four-Bar Flapping Wing Mechanism, IX ECCOMAS Thematic Conference on Smart Structures and Materials, SMART 2019 ECCOMAS-2019, Paris France, ISBN: 978-84-949194-6-6.

[12] Withers, P. C. 1981. An aerodynamic analysis of bird wings as fixed aerofoils. Journal of Experimental Biology, 90(1), 143-162.

[13] Nabawy M. R. A., Crowther, W. J. 2017. The role of the leading edge vortex in lift augmentation of steadily revolving wings: a change in perspective. J. R. Soc. Interface.1420170159, doi: 10.1098/rsif.2017.0159.

[14] Polhamus, E. C. 1966. A concept of the vortex lift of sharp-edge delta wings based on a leading-edge-suction analogy. NASA Langley Research Center; Hampton, VA, United States, Document ID: 19670003842.

[15] Muir Rowan, E., Arredondo-Galeana, A., Viola Ignazio, M. 2017. The leading-edge vortex of swift wing-shaped delta wings. R. Soc. open sci.4170077

[16] Hamdani, H., Sun, M. 2000. Aerodynamic forces and flow structures of an airfoil in some unsteady motions at small Reynolds number. Acta Mech. 145, 173–187, doi: 10.1007/BF01453651.

[17] Lai, J. C. S., Platzer, M. F. 1999. Jet characteristics of a

plunging airfoil. AIAA Journal, 37(12), 1529–1537, doi: 1080/19942060.2015.1004820.

[18] Deng, S., Xiao, T. 2016. Effect of flexion on the propulsive performance of a flexible flapping wing. Proceedings of the Institution of Mechanical Engineers, Part G: Journal of Aerospace Engineering, 230(12), 2265–2273, doi: 10.1177/0954410015623304.

[19] Kang, C., Aono, H., Cesnik, C. 2011. Effects of flexibility on the aerodynamic performance of flapping wings. J Fluid Mech 689: 32–74, doi: 10.1017/jfm.2011.428.

[20] Kolomenskiy, D., Moffatt, H., Farge, M., Schneider, K. 2011. Two-and three-dimensional numerical simulations of the clap–fling–sweep of hovering insects. J. Fluids Struct., 27, 784–791, doi: 10.1017/S0022112098002523.

[21] Liu, H., Kawachi, K. 1998. A numerical study of insect flight. J. Comput. Phys. 146 (1), 124–156, doi: 10.1006/jcph.1998.6019.

[22] Ramamurti, R., Sandberg, W. C. 2007. A Computational Investigation of the Three-Dimensional Unsteady Aerodynamics of Drosophila Hovering and Maneuvering. Journal of Experimental Biology, 210, pp. 881-896, doi: 10.1006/jcph.1998.6019.

[23] Dickinson, M. H., Lehmann, F. O., Sane, S. P. 1999. Wing rotation and the aerodynamic basis of insect flight. Science 284, 1954-1960, doi: 10.1126/science.284.5422.1954.

[24] Aono H., Liu H. 2008. A Numerical Study of Hovering Aerodynamics in Flapping Insect Flight. In: Kato N., Kamimura S. (eds) Bio-mechanisms of Swimming and Flying. Springer, Tokyo, doi: 10.1007/978-4-431-73380-5_15

[25] De Croon, G. C. H. E., Percin, M., Remes, B. D. W., Ruijsink, R., Wagter, C. D. 2016. The DelFly – design, aerodynamics, and artificial intelligence of

a flapping wing robot. Netherlands: Springer, doi: 10.1007/978-94-017-9208-0.

[26] Mayo, D. B., Lankford, J. L., Benedict, M., Chopra, I. 2015. Experimental and computational analysis of rigid flapping wings for micro air vehicles, Journal of Aircraft, Vol. 52, No. 4, doi: 10.1177/1756829316646640.

[27] Young, J., Lai, J. C. S., Germain, C. 2008. Numerical simulation and parameter variation of insect wing motion based on dragonfly hovering. AIAA Journal, 46(4), 918– 924, doi: 10.2514/1.31610.

[28] Sahai, R., Galloway, K. C., Karpelson, K., Wood, R. J. 2012. A Flapping–Wing Micro Air Vehicle with Interchangeable Parts for System Integration Studies. IEEE/RSJ International Conference on Intelligent Robots and Systems, Algarve, Portugal, 2012, pp. 501, 506, doi: 10.1109/IROS.2012.6386058.

[29] Bejgerowski, W., Ananthanarayanam, A., Mueller, D., Gupta, S. K. 2009. Integrated Product and Process Design for a Flapping Wing Drive-Mechanism, ASME Journal of Mechanical Design, Vol. 131, No. 6, 2009, pp. 1006, 1009, doi:10.1115/1.3116258.

[30] Abdulrahim, M. 2004. Dynamic characteristics of morphing micro air vehicles, thesis for Master of Science, Department Mechanical and Aerospace Engineering, University of Florida.

[31] Albertani, R., Stanford, B., Hubner, J.P., Ifju, P. G. 2007. Aerodynamic Coefficients and Deformation Measurements on Flexible Micro Air Vehicle Wings. Exp Mech 47, 625–635, doi: 10.1007/s11340-006-9025-5.

[32] Shyy, W., Ifju, P., Viieru, D. 2005. Membrane Wing-Based Micro Air Vehicles. Applied Mechanics Reviews, 58(4), 283. doi:10.1115/1.1946067

[33] Cleaver, D. J., Calderon, D. E., Wang, Z., Gursul, I. 2016. Lift enhancement through flexibility of plunging wings at low Reynolds numbers. Journal of Fluids and Structures, 64, 27–45. doi:10.1016/j.jfluidstructs.2016.04.004

[34] Nakata, T., Liu, H. 2012. A fluid-structure interaction model of insect flight with flexible wings. Journal of Computational Physics, 231(4), 1822–1847. doi:10.1016/j.jcp.2011.11.005

[35] Gopalakrishnan, P., Tafti, D. K. 2010. Effect of Wing Flexibility on Lift and Thrust Production in Flapping Flight. AIAA Journal, 48(5), 865–877. doi:10.2514/1.39957

[36] Knoller, R. 1909. Die Gesetze des Luftwiderstandes. Flug- und Motortechnik (Wien), Vol. 3, No. 21, pp. 1–7.

[37] Betz, A. 1912. Ein Beitrag zur Erklaerung des Segelfluges. Zeitschrift fur Flugtechnik und Motorluftschiffahrt, Vol. 3, 1912, pp. 269–272.

[38] Katzmayr, R. 1996. Effect of Periodic Changes of Angle of Attack on Behavior of Airfoils. NACA TM 147, Document ID: 19930083152.

[39] Ellington, C. P. 1984. The Aerodynamics of Hovering Insect Flight. I. The Quasi-Steady Analysis. Phil. Trans. R. Soc. Lond. B, February 24, Vol. 305, pp. 1-15, doi:10.1098/rstb.1984.0049.

[40] Ellington, C. P. 1984. The Aerodynamics of Hovering Insect Flight. II. Morphological Parameters. Phil. Trans. R. Soc. Lond. B, February 24, 1984, Vol. 305, pp. 17-40, doi:10.1098/rstb.1984.0050.

[41] Ellington, C. P. 1984. The Aerodynamics of Hovering Insect Flight. III. Kinematics. Phil. Trans. R. Soc. Lond. B, February 24, 1984, Vol. 305, pp. 41-78, doi:10.1098/rstb.1984.0051.

[42] Ellington, C. P. 1984. The Aerodynamics of Hovering Insect Flight. IV. Aerodynamic Mechanisms. Phil. Trans. R. Soc. Lond. B, February 24, Vol. 305, pp. 79-113, doi:10.1098/rstb.1984.0052.

[43] Ellington, C. P. 1984. The Aerodynamics of Hovering Insect Flight. V. A Vortex Theory. Phil. Trans. R. Soc. Lond. B, February 24, 1984 Vol. 305, pp. 115-144, doi:10.1098/rstb.1984.0053.

[44] Ellington, C. P. 1984. The Aerodynamics of Hovering Insect Flight. VI. Lift and Power Requirements. Phil. Trans. R. Soc. Lond. B, February 24, Vol. 305, pp. 145-181, doi:10.1098/rstb.1984.0054.

[45] Ellington, C. P, van den Berg, C., Willmott, A. P., Thomas, A. L. R. 1996. Leading-edge vortices in insect flight. Nature 384, 626–630, doi:10.1038/384626a0.

[46] Lehmann, F. O., Sane, S. P., Dickinson, M. 2005. The aerodynamic effect of wing-wing interaction in flapping insect wings, Journal of Experimental Biology, Vol. 208, pp.3075-3092.

[47] Muijres, F. T., Johansson, L. C., Barfield, R., Wolf, M., Spedding, G. R., Hedenstrom, A. 2008. Leading-edge vortices increase lift in bat flight. Science 319:1250–1253, doi: 10.1126/science.1153019.

[48] Combes, S. A., Daniel, T. L. 2003. Into thin air: contributions of aerodynamic and inertial-elastic forces to wing bending in the hawkmoth Manduca sexta. Journal of Experimental Biology 206:2999-3006, doi: 10.1242/jeb.00502.

[49] Sane, S. P., Dickinson, M. H. 2002. The aerodynamic effects of wing rotation and a revised quasi-steady model of flapping flight. J Exp Biol. 2002;205(Pt 8):1087-1096

[50] Muniappan, A., Baskar, V., Duriyanandhan, V. 2005. Lift and thrust characteristics of flapping wing Micro Air Vehicle (MAV). AIAA2005-1055, 43rd AIAA Aerospace Sciences Meeting and Exhibit, Reno, Nevada, Jan. 10–13, doi: 10.2514/6.2004-6331.

[51] Liu, H., Wang, X., Nakata, T., Yoshida, K. 2012. Aerodynamics and flight stability of a prototype flapping micro air vehicle. 2012 ICME International Conference on Complex Medical Engineering (CME), doi:10.1109/iccme.2012.6275676

[52] Dielectric manufacturing, 2020. ABS (Acrylonitrile-Butadlene-Styrene). Retrieved from https://dielectricmfg.com/knowledge-base/abs/

[53] Pytel, A., Kiusalaas, J. 2010. Engineering Mechanics, SI Edition prepared by Ishan Sharma, Indian Institute of Technology, Kanpur, ISBN-13: 978-0-495-29563-1.

[54] Beer, F., E. Johnston 1962. Dinamik. Birsen Yayınevi. ISBN: 975 511 048 8

[55] Overview of materials for High Density Polyethylene (HDPE), Injection Molded, 2020. Retrieved from http://www.matweb.com/search/datasheet_print.aspx?matguid=fce23f90005d4fbe8e12a1bce53ebdc8

[56] Shyy, W., Aono, H., Kang, C., Liu, H. 2013. An Introduction to Flapping Wing Aerodynamics, Cambridge University Press, New York, ISBN: 978-1107037267

[57] Pradyumna, S. V., Prateek, R., Vinay, T. D., Raju, B. S. 2015. Design & Analysis of an Elliptical Shaped Low Winger Radio Controlled Airplane. nternational Journal of Engineering Trends and Technology(IJETT), Volume 26 Number 5.